Revisiting the Role of Discharge Products in Li–CO$_2$ Batteries

Jinshuo Zou, Gemeng Liang, Fangli Zhang, Shilin Zhang,* Kenneth Davey, and Zaiping Guo*

Rechargeable lithium-carbon dioxide (Li–CO$_2$) batteries are promising devices for CO$_2$ recycling and energy storage. However, thermodynamically stable and electrically insulating discharge products (DPs) (e.g., Li$_2$CO$_3$) deposited at cathodes require rigorous conditions for completed decomposition, resulting in large recharge polarization and poor battery reversibility. Although progress has been achieved in cathode design and electrolyte optimization, the significance of DPs is generally underestimated. Therefore, it is necessary to revisit the role of DPs in Li–CO$_2$ batteries to boost overall battery performance. Here, a critical and systematic review of DPs in Li–CO$_2$ batteries is reported for the first time. Fundamentals of reactions for formation and decomposition of DPs are appraised; impacts on battery performance including overpotential, capacity, and stability are demonstrated; and the necessity of discharge product management is highlighted. Practical in situ/operando technologies are assessed to characterize reaction intermediates and the corresponding DPs for mechanism investigation. Additionally, achievable control measures to boost the decomposition of DPs are evidenced to provide battery design principles and improve the battery performance. Findings from this work will deepen the understanding of electrochemistry of Li–CO$_2$ batteries and promote practical applications.

1. Introduction

The ubiquitous burning of fossil fuels contributes significantly to greenhouse gases that aggravate the climate change and negatively affect the world economy.[1] As substitutes for fossil fuels, renewable and low-carbon energy sources are considered to contribute to a more sustainable future.[2] Among them, rechargeable batteries are increasingly seen as a technology for efficient utilization of sustainable energy sources.[3] Recently, metal-carbon dioxide (CO$_2$) batteries, including Li–CO$_2$, Na–CO$_2$, and K–CO$_2$, have attracted significant attention and become attractive to support the fast-expanding energy demand because they apply the CO$_2$ recycle to energy storage system and contribute to decarbonization of global energy markets.[4] Metal–CO$_2$ batteries utilizing CO$_2$ in energy storage are potential energy sources for electromobile, Mars exploration, and submarine operation, where CO$_2$ is abundant. Amongst these, Li–CO$_2$ batteries are the most promising candidate because of a high discharge voltage of 2.8 V and theoretical energy density of 1876 W h kg^{-1}.[4b,5]

Li–CO$_2$ batteries were originated from CO$_2$-involved Li–O$_2$ batteries. In 2011, Takechi et al. introduced CO$_2$ to Li–O$_2$ batteries to increase the discharge capacity and energy density.[6] In 2013, Xu et al. developed a Li–CO$_2$ battery with a high discharge capacity of 2500 mAh g^{-1} using an activated carbon-based cathode and ionic liquid electrolyte operated at the temperature of 100 °C, as is shown in **Figure 1**a.[7] After that, research efforts were made to develop highly reversible Li–CO$_2$ batteries with attention to catalyst design, electrolyte engineering, and optimization of device configuration.[8] Generally, during discharge, electrons transfer from the cathode to the absorbed CO$_2$ and react with Li$^+$ ions migrating from Li anode to form discharge products (DPs), including lithium carbonate and amorphous carbon (Li$_2$CO$_3$ and C) based on the reaction, 4Li + 3CO$_2$ ↔ 2Li$_2$CO$_3$ + C. On charge, DPs are expected to be reversibly decomposed to Li$^+$ ions and CO$_2$ molecules.[5b,9]

Despite the progress achieved in Li–CO$_2$ batteries, further development from laboratory-scale to practical application remains restricted because of low reversibility, high voltage polarization, and inadequate lifespan.[10] The limitation to performance development is the decomposition difficulty with DPs during charge.[11] The major DPs, Li$_2$CO$_3$ & C, require a high charge potential of >4.2 V for decomposition because of the thermodynamically stable and electrically insulating nature of Li$_2$CO$_3$.[12] The

J. Zou, G. Liang, F. Zhang, S. Zhang, K. Davey, Z. Guo
School of Chemical Engineering and Advanced Materials
The University of Adelaide
Adelaide, SA 5005, Australia
E-mail: shilin.zhang01@adelaide.edu.au; zaiping.guo@adelaide.edu.au
F. Zhang
Institute for Superconducting & Electronic Materials
University of Wollongong
Wollongong, NSW 2522, Australia

**ADVANCED
SCIENCE NEWS**
www.advancedsciencenews.com

**ADVANCED
MATERIALS**
www.advmat.de
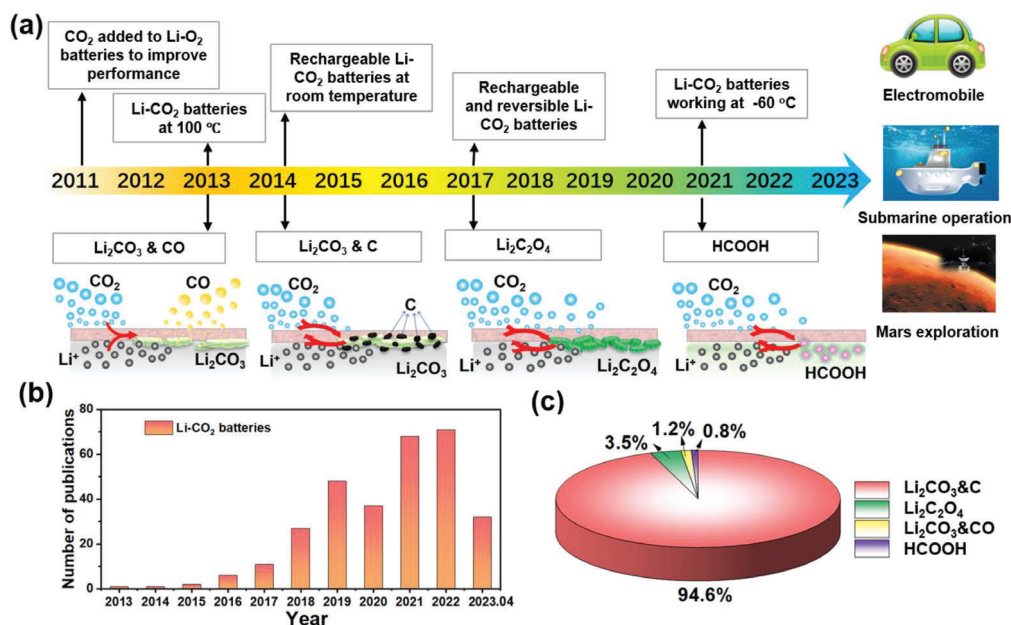
Figure 1. a) Timeline for development of Li–CO₂ batteries and potential applications. b) Research trend in Li–CO₂ batteries. (Updated on 27th April 2023. Key search word used in Web of Science was "Li–CO₂ batteries"). c) Publication distribution for different DPs in Li–CO₂ batteries.

depth of DP decomposition and the accumulation of residues gradually deteriorates the reversibility and cycling stability of Li–CO₂ batteries. In some cases, DPs can be controlled to readily degradable $Li_2C_2O_4$, CO, and HCOOH products in Figure 1a with lowered charge potential and improved energy efficiency during cycling.[13] However, catalysts for $Li_2C_2O_4$ are restricted because only Mo-based catalysts are reported to stabilize $C_2O_4^{2-}$ intermediates. To form HCOOH products, aqueous electrolyte should be used because CO_2 reduction to HCOOH requires proton from electrolyte(s).[14] The CO-related Li–CO₂ system is less reported because CO is not detected in most systems. As is seen in Figure 1b,c, prevalent DPs are Li_2CO_3 & C, and the major practical challenge with Li–CO₂ battery development is the promotion of Li_2CO_3 decomposition. An improved control of DPs is necessary to achieve satisfactory electrochemical performance and activate the inhibited CO_2 electrochemistry in Li–CO₂ batteries.

Previous reviews have summarized recent progress on specific components for Li–CO₂ batteries, including strategies for cathode design, engineering of electrolyte formulas, and functional electrocatalysts, together with methods for anode protection.[4a,5b,15] However, the electrochemical behavior of DPs and formation /decomposition mechanisms received significantly less attention. Additionally, impacts of DPs on electrochemical performance, rational DP controls, and elaborate characterizations, remain lacking. In this review, we critically revisit DPs in Li–CO₂ systems with a focus on problematic formation and decomposition mechanisms, compositions, behaviors, and significance in managing DPs for CO_2 electrochemistry and performance of Li–CO₂ batteries. We begin with the formation and decomposition reactions of DPs, including Li_2CO_3 & C, $Li_2C_2O_4$, Li_2CO_3 & CO and HCOOH. Effects of product type and corresponding mechanism on electrochemical performance are assessed to highlight the significance of DP control. Specifically,

characterization methods such as in situ/operando techniques for product analyses and mechanism understanding are systematically reviewed. We then review control methods for DPs, including cathode, electrolyte, and cell configuration, to tailor Li–CO₂ battery performance. Finally, we present our vision of design principles for DPs, highlight emerging strategies, and examine remaining challenges that govern the overall system efficiency of Li–CO₂ devices.

2. Discharge Product (DP) Formation/Decomposition Mechanisms

The mechanism(s) for DP-related reactions is the operational "heart" for Li–CO₂ batteries. Originating from Li–O₂ batteries, Li–CO₂ batteries are an open system requiring CO_2 as the energy storage medium to the cell that can be constructed as a part of the hybrid battery-fuel cell. During discharge, Li anode releases electrons to the external circuit and generates Li^+ ions that are then transferred to the cathode chamber. The CO_2 reduction occurs at the three-phase interface of CO_2, electrolyte, and the cathode surface, where the CO_2 can be converted to products including Li_2CO_3 & C, $Li_2C_2O_4$, Li_2CO_3 & CO, and HCOOH, with the participation of Li^+ ion and electrons (**Figure 2**). The charge process involves the decomposition of DPs and the release of CO_2 and Li^+ ions. Compared with oxygen reduction reaction (ORR) and oxygen evolution reaction (OER) in Li–O₂ batteries, the dominant CO_2 reduction and evolution are multistep reactions with substantial intermediates that complicate the Li–CO₂ system, especially for analyses of DPs. Therefore, an improved understanding of DP formation during discharge (CO_2 reduction reaction, CRR) and decomposition during charge (CO_2 evolution reaction, CER) is necessary to understand impacts on electrochemical performance of Li–CO₂.
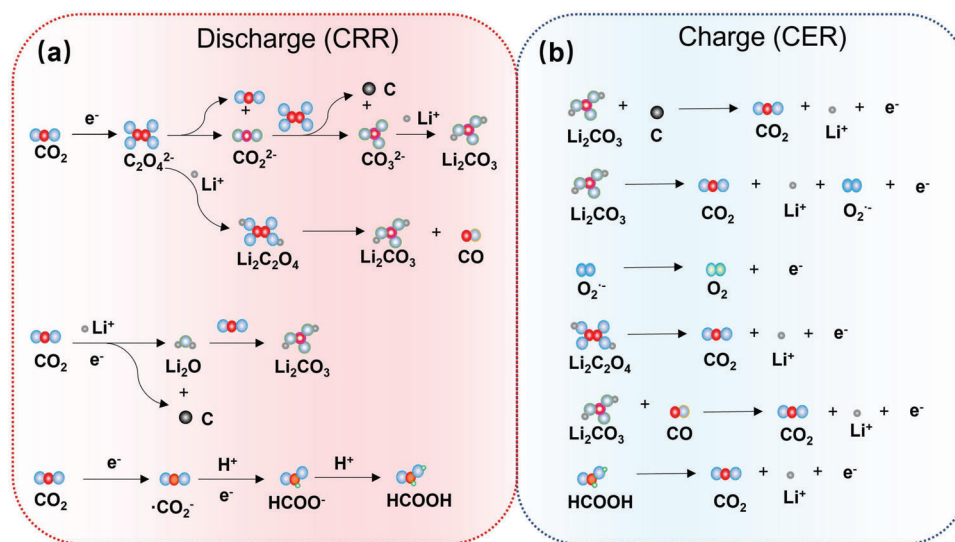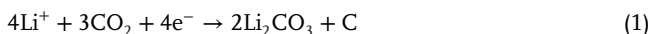
2210671 (2 of 33)

Figure 2. a) Discharge and b) charge mechanism for Li–CO$_2$ batteries.

2.1. Li$_2$CO$_3$ & C Products

### 2.1.1. Formation Pathways for Li$_2$CO$_3$ & C Products

Li$_2$CO$_3$ & C products are generally reported in Li–CO$_2$ batteries with the most accepted discharge route of Equation 1 in aprotic electrolytes. During discharge, Li$_2$CO$_3$ is deposited with amorphous carbon on cathode, synchronously. Hou et al. proposed a disproportionation reaction mechanism for Li$_2$CO$_3$ and C products in Li–CO$_2$ batteries based on mechanisms of Li–O$_2$ batteries.[13a] Specifically, the CRR takes place first with the formation of thermally unstable C$_2$O$_4^{2-}$ intermediate from dissolved CO$_2$ molecules, which involves a two-electron transfer process (Equation 2). The C$_2$O$_4^{2-}$ reacts disproportionately with CO$_2^{2-}$ and CO$_2$ (Equation 3), following which the C$_2$O$_4^{2-}$ couples with CO$_2^{2-}$ to form C and CO$_3^{2-}$, (Equation 4). Li$^+$ ions from the anode then can react with CO$_3^{2-}$ to form Li$_2$CO$_3$, Equation 5. It is concluded that CRR chemistry involves multielectron transfer processes in multiple steps, accompanied by the generation of complicated intermediates. Although identifying reaction intermediates and rate-determining steps in the CRR presents difficulties, Qiao et al. observed oxalate species (C$_2$O$_4^{2-}$) peaks at the beginning of discharge.[16] The C$_2$O$_4^{2-}$ signal then gradually disappears with the emergence of Li$_2$CO$_3$ (1319 cm^{-1}) and C (1587 cm^{-1}) in subsequent reactions based on in situ Raman spectra. These findings are in good agreement with the proposed disproportionation reaction mechanism (Equation 4).

$$4Li^+ + 3CO_2 + 4e^- \rightarrow 2Li_2CO_3 + C \tag{1}$$

$$2CO_2 + 2e^- \leftrightarrow C_2O_4^{2-} \tag{2}$$

$$C_2O_4^{2-} \rightarrow CO_2^{2-} + CO_2 \tag{3}$$

$$C_2O_4^{2-} + CO_2^{2-} \rightarrow 2CO_3^{2-} + C \tag{4}$$

$$2Li^+ + CO_3^{2-} \rightarrow 2Li_2CO_3 + C \tag{5}$$

2.1.2. Nucleation and Growth of Li$_2$CO$_3$ & C Products

The nucleation and growth of Li$_2$CO$_3$ and C are affected by the binding energy between intermediate species and employed catalysts. Similar to the formation mechanisms for Li$_2$O$_2$ in Li–O$_2$ batteries, there are two main routes for Li$_2$CO$_3$ & C nucleation and growth, namely: surface adsorption growth and solvation-mediated growth mechanism.[17] If carbonaceous intermediates have relatively weak binding energy to cathode materials, the Li$_2$CO$_3$ preferentially nucleates in the electrolyte near the cathode surface through a solvation-mediated growth mechanism (**Figure 3**a).[18] The formed Li$_2$CO$_3$ would stack on the cathode surface and forms some specific morphology, for example, self-assembled flower-like structures.[18,19] In contrast, if the binding energy between the catalyst surface and carbonaceous is sufficiently strong, the Li$_2$CO$_3$ layer tends to grow directly on cathode surface via surface adsorption growth mechanism to form uniform and conformal morphology.

Lian et al. reported the growth of Li$_2$CO$_3$ tends to be solvation-mediated growth mechanism on Co$_3$O$_4$-based cathode.[19a] This mechanism eventually leads to the generation of massive shape discharge products. Ma et al. prepared MnOOH arrays on stainless-steel (SS) mesh cathode for Li–CO$_2$ batteries.[18] They reported the product nucleation and growth on MnOOH follow surface adsorption growth with uniform and conformal morphology because of the high adsorption energy of covalent bond between Li@Li$_2$CO$_3$ and O@MnOOH (-4.31 eV). Ultrafine Li$_2$CO$_3$ (≈5 nm) are uniformly embedded into the carbon matrix, which significantly enlarges the contact interface of the two products, facilitates electron transmission through DPs, and promotes CO$_2$ evolution during charge. Wang et al. studied the product growth mechanism on a RuO$_2$@TiO$_2$ catalyst and found the Li$_2$CO$_3$ growth mechanism can be modulated, as is shown in **Figure** 3b–g.[19b] TiO$_2$ surface has a relatively strong adsorption energy to CO$_2$. Thereby, the CO$_2$ can readily be captured by the surface of TiO$_2$ and react with Li$^+$ to form Li$_2$CO$_3$ via surface adsorption growth.

ADVANCED
SCIENCE NEWS
www.advancedsciencenews.com

ADVANCED
MATERIALS
www.advmat.de
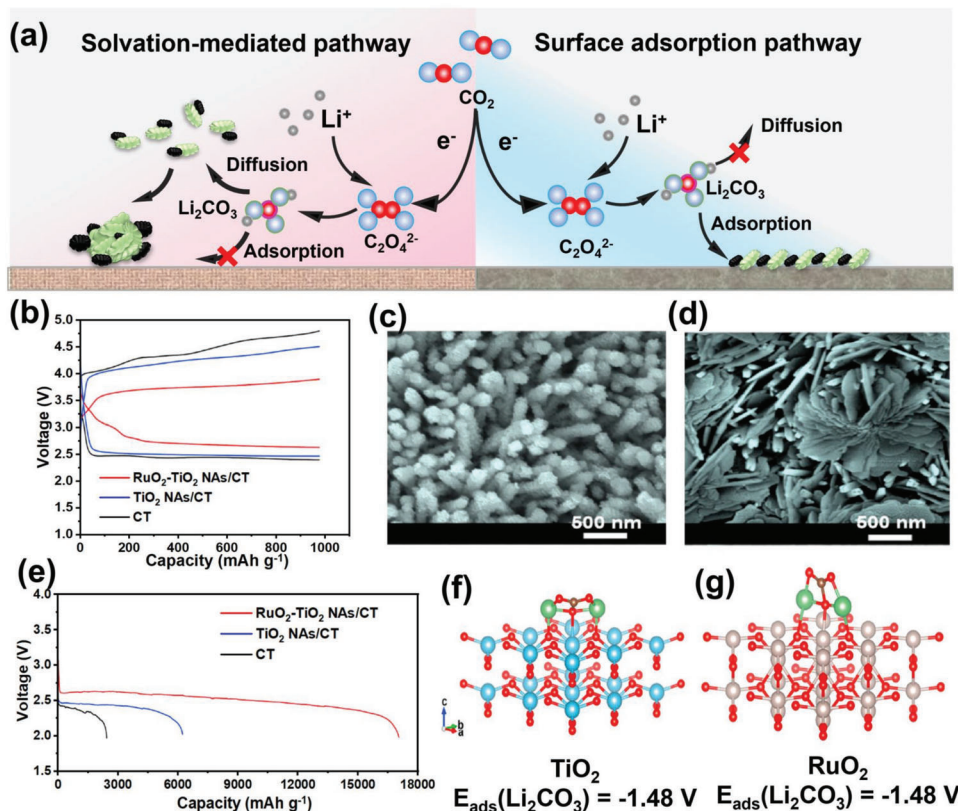
Figure 3. a) Growth mechanisms for Li_2CO_3 & C products in Li–CO_2 batteries. b) Galvanostatic discharge–charge (GDC) profiles for RuO_2 nanoparticles decorated TiO_2 nanowire arrays on carbon textiles (RuO_2–TiO_2 NAs/CT), TiO_2 NAs/CT, and CT of the first cycle. SEM images of c) TiO_2 NAs/CT and d) RuO_2–TiO_2 NAs/CT cathodes observed after discharge to 2000 mAh g^{-1}. e) Galvanostatic discharge profiles for RuO_2–TiO_2 NAs/CT, TiO_2 NAs/CT, and CT. Optimized structures and corresponding binding energy for Li_2CO_3 on f) TiO_2 and g) RuO_2. b–g) Reproduced with permission.[19b] Copyright 2020, Elsevier.

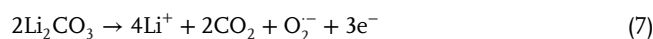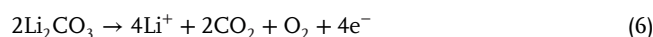Because of the weaker adsorption ability of RuO_2 on Li_2CO_3, the generated Li_2CO_3 is more readily released from the surface of RuO_2 during charge and diffused into the electrolyte, resulting in a solvation-mediated growth mechanism of DPs together with a boosted discharge capacity of 16, 727 mAh g^{-1}.[19b]
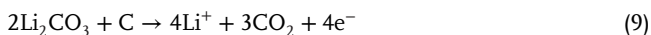
The catalyst design offers a feasible approach to tune the growth mechanism of DPs through either the solvation-mediated growth or the surface adsorption growth mechanism. However, DPs formed through solvation-mediated growth mechanism with flowerlike morphologies tend to be thick and large which is disadvantageous for the following charge reactions.[19b] Meanwhile, the surface adsorption growth mechanism with thin but conformal layer DPs can result in low capacity of batteries. Therefore, a balance between the high capacity and the energy efficiency is necessary in cathode design for Li–CO_2 batteries.

2.1.3. Decomposition Mechanism for Li_2CO_3 & C Products

Theoretically, CER during the charge of Li–CO_2 batteries can be considered as the reverse reaction of CRR (Equation 1), in which CO_2 at the cathode, and metallic Li at the anode, are respectively regenerated. Functional catalysts are favored to boost the sluggish decomposition kinetics of Li_2CO_3. An extensive understanding

of the decomposition mechanism for DPs is crucial therefore to develop well-selected catalysts to satisfy stringent requirements, especially for CER. Recently Qiao et al. investigated charge reactions by in situ Raman and demonstrated that Au-based electrocatalysts only allow the sole decomposition of Li_2CO_3 (Equation 6) which requires high charge potentials ($E^0 = 3.82$ V vs Li/Li$^+$).[16] This conversion involves the formation of $O_2^{.-}$ radicals (Equations 7 and 8) which may react with electrolyte solvents and decrease battery reversibility and stability. However, Ru-based electrocatalysts promote concurrent decomposition between Li_2CO_3 and amorphous carbon species to form Li and CO_2. They found the Raman peak intensity for Li_2CO_3 at 1085 cm^{-1} and G-band of carbon at 1587 cm^{-1} decreases synchronously with the increase of linear scan potential from 3.0 to 4.5 V after a galvanostatic discharge (Equation 9). In this process, CO_2 is the only gaseous product, and rechargeable /irreversible Li–CO_2 batteries transfer to reversible batteries with thermodynamic equilibrium potential of 2.8 V versus Li/Li$^+$. Although the catalytic mechanism for Ru in CO_2 evolution remains unclear, the battery performance is no longer limited by irreversibility.

$$2Li_2CO_3 \rightarrow 4Li^+ + 2CO_2 + O_2 + 4e^- \tag{6}$$

$$2Li_2CO_3 \rightarrow 4Li^+ + 2CO_2 + O_2^- + 3e^- \tag{7}$$

**ADVANCED
SCIENCE NEWS**

www.advancedsciencenews.com

**ADVANCED
MATERIALS**

www.advmat.de

$$O_2^- - e^- \rightarrow O_2 \tag{8}$$

$$2Li_2CO_3 + C \rightarrow 4Li^+ + 3CO_2 + 4e^- \tag{9}$$

Generally, the Li_2CO_3 is crystallized and/or amorphous depending on electrochemical environment(s). In crystallized Li_2CO_3, the 2p orbitals from the C atom combine with the 2p orbitals of three O atoms and form stable π orbitals of carbonate, which are perpendicular to the triangle plane.[20] As a result, the breakdown of crystalized carbonate is likely the most difficult. However, it is facile for amorphous Li_2CO_3 to be decomposed as C–O bonds are not uniformly distributed. Xiao et al. observed a two-stage charge voltage profile on CNT electrodes after initial charge polarization.[21] The first stage is proposed to be the decomposition of ultrafine crystal and amorphous Li_2CO_3, which is sensitive to the applied current density. The second stage with high overpotential corresponds to the decomposition of blockage of transport channels and accumulated side products. However, unlike product nucleation and growth, there is no direct confirmatory evidence for the decomposition mechanism. Details for Equation 9 remain sophisticated and require more in-depth study to determine mechanisms for the development of high-performance Li–CO$_2$ batteries.

2.2. Li$_2$C$_2$O$_4$ Products

Numerous research efforts have been devoted to understanding the formation/decomposition of DPs for prolonged battery lifespan and reversible capability. The theme of this has been to modulate the formation of intermediates. Most studies report that Li_2CO_3 and C are the final DPs and that the $C_2O_4^{2-}$ generated through the route of Equation 2 is an intermediate during CO_2 reduction because of the thermally unstable property of $Li_2C_2O_4$. However, if $C_2O_4^{2-}$ species are stabilized by catalysts, corresponding disproportionation reactions in Equations 3–5 would be suppressed and the $Li_2C_2O_4$ phase becomes the final DPs instead of Li_2CO_3. Compared with insulating and insoluble Li_2CO_3 products, this environmentally friendly oxalate salt species is more favorable because the potential for CO_2 reduction to $C_2O_4^{2-}$ is ca. -0.03 V versus normal hydrogen electrode (NHE) and the oxidation of $C_2O_4^{2-}$ to CO_2 occurs at +0.81 V versus NHE.

In 2017, Hou et al. first reported the MO$_2$C-CNT catalyst and pointed out that $Li_2C_2O_4$ was the sole product formed during discharge (**Figure 4**a).[13a] In addition, they reported that the charge potential was effectively reduced to less than 3.5 V with a high round-trip efficiency of 77%. They attributed the stabilization of $C_2O_4^{2-}$ species to the coupling of Mo with O in $C_2O_4^{2-}$ through coordinative electron transfer (Equation 10). Where after, Zhou et al. used ultrafine Mo$_2$C nanoparticles anchored on a carbon nanotube (CNT) cloth as the cathode.[13d] By comparing charge density differences of $Li_2C_2O_4$ on Mo$_2$C and CNT surfaces (**Figure** 4b), they confirmed Mo$_2$C could stabilize the $Li_2C_2O_4$ by transferring outer electrons to O atoms in $Li_2C_2O_4$. This hybrid catalyst exhibited higher capacity of 3,415 µAh cm^{-2} and lower overpotential of 0.65 V (**Figure** 4c,d). Both $Li_2C_2O_4$ and Mo–O species are detected via in situ Raman spectra, as shown in Figure 4e. Yang et al. theoretically postulated reaction mechanisms for MO$_2$C catalysts via first-principles density functional

theory (DFT) computation.[13b] They confirmed that disproportionation reactions of Equations 3–5 for Li_2CO_3 were inhibited because of the increased free energy change of the split reaction, resulting in well-preserved $Li_2C_2O_4$ products. Additionally, β-MO$_2$C (001) and (101) catalyst surfaces exhibited the lowest Gibbs free energy change for $Li_2C_2O_4$ nucleation and the lowest overpotential for discharge. Electron transfers were found between $Li_2C_2O_4$ and MO$_2$C surfaces based on Bader charge analysis.

More important however is that charge reaction kinetics at the surface of Mo$_2$C are accelerated together with a lowered thermodynamic equilibrium potential (2.8 V vs Li/Li$^+$). Based on the proposed charging mechanism where $Li_2C_2O_4$ serves as main product, $Li_2C_2O_4$ can be readily converted back to Li$^+$ ions and release CO_2 molecular via Equation 11 by electron transmission to external circuit without any residual(s) or side reaction(s). Li–CO$_2$ batteries therefore exhibit excellent reversibility and stability when $Li_2C_2O_4$ forms as DPs. Notably, Wu et al. reported that, unlike previous studies in which Mo$_2$C was reported to stabilize of intermediate oxalate species, synthesized graphene nanoplatelets/β-Mo$_2$C catalyst followed a conventional reaction mechanism with formation of Li_2CO_3 in high-dielectric N,N-dimethylacetamide electrolyte, despite it still shows improved electrochemical performance.[22] The intermediate stabilizing effect of Mo-based components in Li–CO$_2$ batteries appears important for further investigation.

$$C_2O_4^{2-} + 2Li^+ + Mo_2C \rightarrow Li_2C_2O_4 - Mo_2C \tag{10}$$

$$Li_2C_2O_4 \rightarrow 2Li^+ + 2CO_2 + 2e^- \tag{11}$$
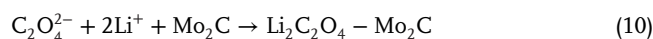
However, until now, only Mo-based catalysts, such as Mo$_2$C and MoN, have been reported for stabilizing $Li_2C_2O_4$ species via Mo–O bond.[13d,22,23] In the area of electrocatalytic CO_2 reduction, metal-organic frameworks (MOF), cobalt phthalocyanine (CoPc), or copper-based catalysts, were found to stabilize $C_2O_4^{2-}$ species.[24] With reasonable design, these catalysts might also be applied to stabilize $Li_2C_2O_4$ products in Li–CO$_2$ batteries.

2.3. Li$_2$CO$_3$ & CO Products

Another promising DP in aprotic Li–CO$_2$ is CO, which favors highly reversible Li–CO$_2$ batteries with low overpotential. In 2013, Xu et al. were the first to report that $Li_2C_2O_4$ intermediates could be converted to Li_2CO_3 and CO at high temperatures.[7] The measured discharge potential surpassed the theoretical equilibrium potential value, demonstrating the proposed process of Equation 12 is significantly complicated, or indeed, partially incorrect. Electrocatalysts played a key role in controlling electrochemical reactions and altering final reduction products of CO_2 to CO because of various electrocatalytic selectivity. Xie et al. designed a 3D porous fractal Zn material as the first Li–CO$_2$ battery system with the fuel-gas CO as the gaseous reduction product.[25] After discharge, no amorphous C was detected and therefore the related discharge reaction can be proposed as Equation 13. The CO generation is adjustable, with a maximum Faradaic efficiency (FE) of 67% at the applied current of 0.1 mA. However, it should be noted the generation of CO is accompanied with

**ADVANCED
SCIENCE NEWS**

www.advancedsciencenews.com

**ADVANCED
MATERIALS**

www.advmat.de
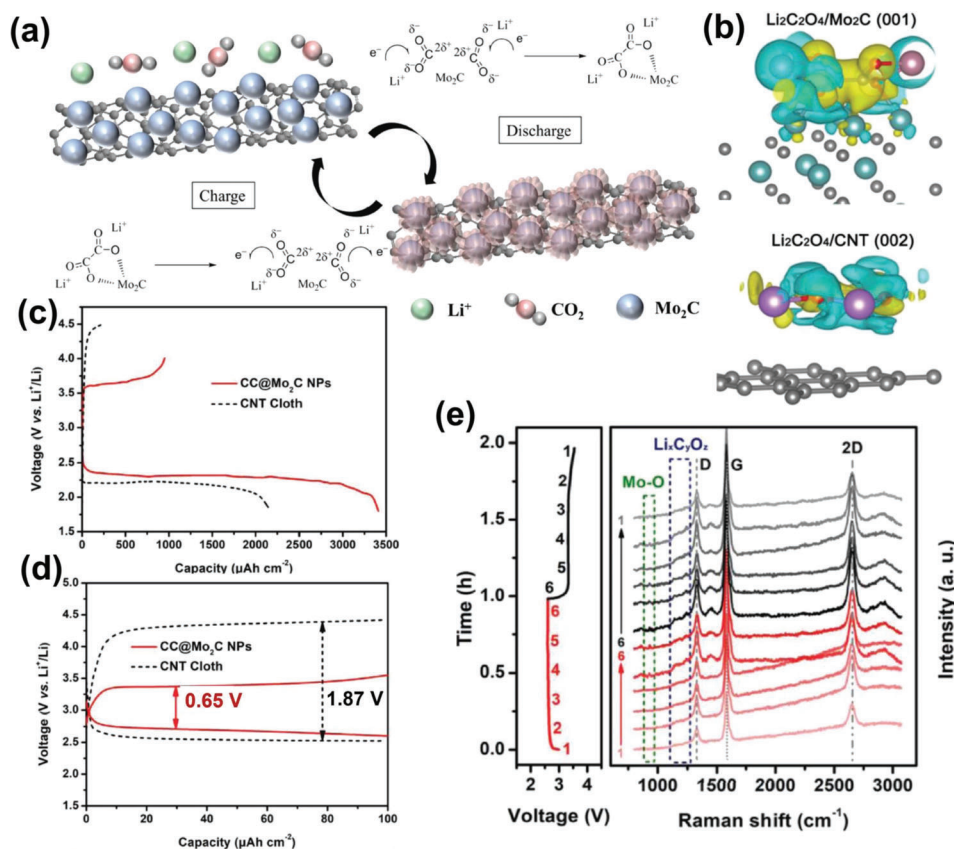
Figure 4. Summary of $Li_2C_2O_4$ product-based Li–CO_2 batteries. a) Schematic illustration of discharge and charge reactions on Mo_2C/CNTs catalysts. Reproduced with permission.[13a] Copyright 2017, Wiley. b) Charge density difference of $Li_2C_2O_4$ adsorbed on Mo_2C (001) surface and CNTs (002) surface. c) GDC profiles for Mo_2C nanoparticles anchored on a carbon nanotube (CNT) cloth (CC@Mo_2C NPs) and CNT cloth at the current density of 50 μA cm^{-2}. d) GDC profiles for CC@Mo_2C NPs and CNT cloth within initial capacity of 100 μA cm^{-2}. e) In situ Raman spectra of CC@Mo_2C NPs at 12 selected states during cycling at 20 μA cm^{-2}. Reproduced with permission.[13d] Copyright 2019, Wiley.

Li_2CO_3. FE decreases when solid Li_2CO_3 products accumulate and cover the cathode surface, leading to reduced battery performance. Zhao et al. obtained direct spectroscopic evidence of CO_2^{-}, CO, and Li_2CO_3) by using Cu-coated Au (Cu$_{ML}$@Au) catalysts. They proposed CO product-related mechanism in Equation 13 via in situ surface-enhanced Raman spectroscopy (SERS) and theoretical computation.[26] They highlighted that CRR via conventional Equation 1 might be difficult in the catalyst because of sluggish chemical steps involved (e.g., dimerization of two CO_2^{-} intermediates), which can be determined by near-Fermi level d-orbital states of the electrocatalyst and cation type.

$$2Li + 2CO_2 \rightarrow Li_2C_2O_4 \rightarrow Li_2CO_3 + CO \tag{12}$$

$$2Li^+ + 2CO_2 + 2e^- \rightarrow Li_2CO_3 + CO \tag{13}$$
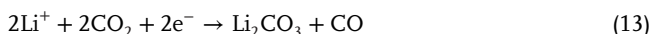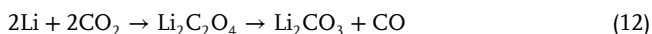
The CO in aprotic Li–CO_2 battery represents a practically promising product because of its wide application in industry, including Fischer–Tropsch synthesis, pharmaceuticals, and reduction of ores.[27] High-performance catalysts for electrochemical CO_2 reduction, such as Au, Ag, Zn, and Cu can be employed in Li–CO_2 batteries. However, regarding the CO formation mechanisms, in electrochemical CO_2 reduction to CO in aqueous electrolytes, protons are indispensable for the formation of intermediates such as *COOH, which is not applicable for the aprotic electrolyte in Li–CO_2 batteries.[28] Therefore, CO formation in Li–CO_2 batteries needs to be determined with caution.

2.4. HCOOH Products

In cathode electrodes, most DPs reported in Li–CO_2 batteries are insoluble with different morphology, such as Li_2CO_3, C, or $Li_2C_2O_4$, ranging from hundreds of nanometers to micrometers in size. Soluble liquid product might be ideal because products can timely desorb from the active site and sufficient contact between reactants and catalysts ensures completed decomposition. Amongst the diverse liquid CO_2 reduction products (e.g., formic acid, methanol, ethanol, and formaldehyde), formic acid is attractive and practical because it is the most kinetically accessible and many CO_2 reduction catalysts (such as Sn, Bi, Pd, In, Co) have high formic acid selectivity.[29] However, the generation of formic acid requires protons commonly provided by aqueous electrolytes, which may limit the application in aprotic batteries.[30]

ADVANCED
SCIENCE NEWS

www.advancedsciencenews.com

ADVANCED
MATERIALS

www.advmat.de
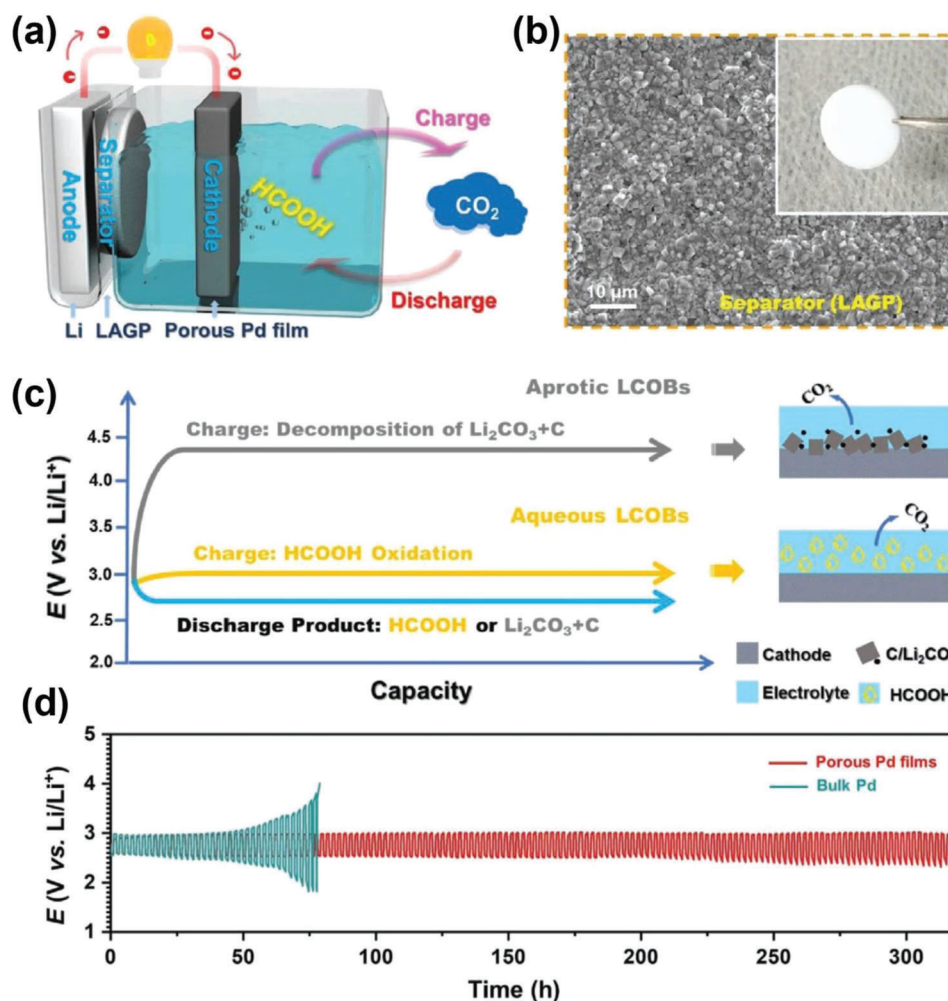
Figure 5. Summary of HCOOH product-based Li–CO_2 batteries and performance. a) Schematic illustration of aqueous Li–CO_2 batteries. b) SEM image of the $Li_{1+x}Al_xGe_{2-x}(PO_4)_3$ (LAGP) separator, the inset is the photograph. c) Comparison between aprotic and aqueous Li–CO_2 batteries. d) Long-term cycling test for porous Pd-film and bulk Pd at 0.2 mA cm^{-2}. Reproduced with permission.[13c] Copyright 2021, Wiley.

Recently, to create an aqueous environment for producing formic acid, Xue et al. used a solid-state electrolyte (SSE) of $Li_{1+x}Al_xGe_{2-x}(PO_4)_3$ (LAGP) as a separator between the aqueous cathode chamber and the aprotic anode chamber which only allows the migration of Li$^+$ ion.[13c] As is seen in the cathode chamber shown in **Figure 5**, nanoporous Pd films were used as catalysts for the reversible reactions (Equation 14), in which thermodynamic equilibrium potential for formic acid generation and decomposition is 2.80 V versus Li/Li$^+$. In this design, formic acid was detected with high selectivity (FE = 90%) and therefore active sites are timely released on catalysts. In addition, the battery can stably cycle for more than 300 h with the low charge potential of 2.99 V, which is promising for practical energy storage and conversion.

$$CO_2 + 2H^+ + 2Li \leftrightarrow HCOOH + 2Li^+ \qquad (14)$$
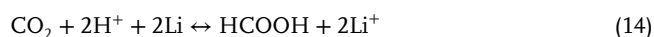
The LAGP separator-involved design enables the reduction of CO_2 in an aqueous electrolyte without affecting the Li$^+$ deposition and releases at the anode. Via this strategy, more efficient and inexpensive catalysts such as Sn and Bi can be applied to Li–CO_2 batteries. However, side reactions, including hydrogen evolution reaction (HER) and CO evolution reaction (CORR), can lower selectivity and cause catalyst degradation.[31] Another problem is the local pH change during electrolysis caused by the consumption of protons or the release of OH$^-$, which may affect the formic acid selectivity.[32] Generally, the CO_2 reduction products tend to be formic acid when the electrolyte pH is lower than 3.75. With an increase of pH, the CO reduction pathway toward formate becomes thermodynamically favored compared with that of formic acid products. When the pH increases to above 7, the standard redox potential for CO_2 reduction to formate reaction is even lower than that of HER.[30a] In addition, electrolyte with high alkaline concentrations can suppress by-products such as CO, H$_2$, and CH$_4$ because of their dependence on proton concentration.[33] Furthermore, high pH electrolyte may result in improved selectivity toward more complex discharge products, such as ethylene and ethane.[34] These gases can be released instead of being oxidized to CO_2 during charge, which decreases the reversibility of Li–CO_2 batteries. Therefore, to achieve excellent stability, the

ADVANCED
SCIENCE NEWS
www.advancedsciencenews.com

ADVANCED
MATERIALS
www.advmat.de
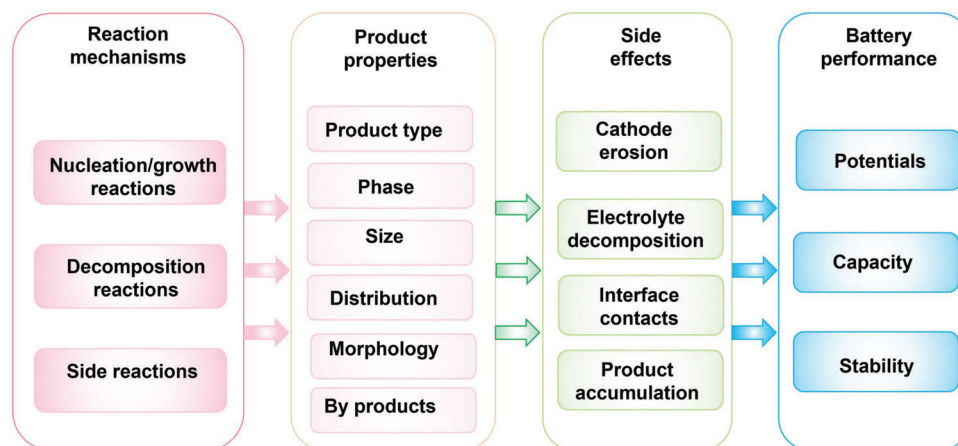
Figure 6. Impacts of discharge/charge mechanisms and DP properties on electrochemical performance.

effect of local pH change should be minimized in this aqueous system. Because the electrolyte pH increase in the cathode chamber is not sufficiently compensated by the SSE separator, ion-exchange membranes such as Nafion membranes can be considered to allow the migration of H^+ or OH^- ions and balance the pH.[35] Another practical strategy is the utilization of electrolyte with high buffer capacity to alleviate the pH change and ensure the battery stability.

3. Effects of DPs on Electrochemical Performance

Despite significant research efforts have been devoted to the Li–CO_2 electrochemistry, the electrochemical performance of current Li–CO_2 batteries still needs to be boosted for any practical application because of the decomposing difficulty of stable DPs and the cathode, or electrolyte decay at high charge potential. **Table 1** presents a comparative summary of the typical Li–CO_2 batteries classified by-product type. Although $Li_2C_2O_4$, CO, or HCOOH-based Li–CO_2 batteries usually present relatively "good" performance, Li_2CO_3 and C are the final DPs in most Li–CO_2 systems. Properties of DPs, determined by CO_2 reduction mechanisms and the nucleation /growth affect the cathode, the electrolyte, and the interface contact, which is critical to electrochemical performance (**Figure 6**). In this section, the effects of DPs in determining electrochemical performance are critically assessed.

3.1. Discharge/Charge Potential as Affected by DPs

3.1.1. Discharge Potentials

Thermodynamic discharge potential (reversible potential) mainly depends on the CO_2 reduction reactions of **Table 2** according to the isothermal relation of Gibbs free energy and electromotive force, namely: $\Delta G = -nFE$. Generally, reactions for producing Li_2CO_3-based products correspond to higher discharge potentials because of the large Gibbs free energy change ($\Delta_f G^0(Li_2CO_3) = $ -1132.12 kJ mol^{-1}), compared with that of Li_2O based product related reactions ($\Delta_f G^0(Li_2O) = $ -561.2 kJ mol^{-1}).[16] The mechanism that involves the reduction of O_2 or CO corresponds to high

thermodynamic discharge potentials of >3.7 V versus Li/Li^+, evidencing the existence of O_2 and CO impurities can result in positive effects on the improvement of discharge potential and energy efficiency.[53] Among the solid DP-related mechanisms, the formation of $Li_2C_2O_4$ with a relatively high equilibrium discharge potential (>3 V vs Li/Li^+) is promising as the following charge process requires lower overpotential. The discharge potential for the formation of $Li_2C_2O_4$ on Mo_2C catalyst can be increased by ≈0.2 V compared with Li_2CO_3 product on CNT-cloth within an initial capacity of 100 μAh cm^{-2}.[13d]

However, the discharge potential is likely, practically, affected by some external factors.[54] Fundamentally, DP formation is itself an electrochemical reaction that depends strongly on the corresponding electrochemical environment. Reaction pathway changes when electrochemical environments do not favor the nucleation and formation of Li_2CO_3 and C. For example, Qiao et al. detected a Li_2O intermediate via reducing the electrolyte concentration (50 × 10^{-3} M) and the CO_2 partial pressure (CO_2/Ar, 1:5 v/v) with an extended discharge capacity of 20 μAh.[16] Raman peaks for Li_2O at 520 cm^{-1} gradually appear when the discharge voltage falls to 1.8 V. This phenomenon is in all probability because of the limited mass transfer in the decreased Li^+ ion and CO_2 partial pressure, leading to Li_2O accumulation at a low discharge potential. Based on theoretical thermodynamic computation, the Li_2O-related mechanism is proposed as Equations 15 and 16. The Li_2O can react further with adsorbed CO_2 and generate Li_2CO_3. Although final products are Li_2CO_3 + C, more complex intermediates can be generated and the discharge potential can only reach 1.8 V. Therefore, the mass transport problem of Li^+ and CO_2 has significant impacts on the reaction mechanism and the discharge potential.[24]

$$4Li^+ + CO_2 + 4e^- \rightarrow 2Li_2O + C \tag{15}$$

$$2Li_2O + 2CO_2 \rightarrow 2Li_2CO_3 \tag{16}$$
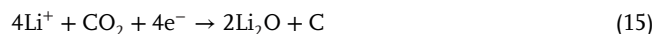
Additionally, the discharge potential can also be influenced by electrolyte and catalyst degradation. The strong oxidizing species can damage cathodes, or electrolytes that will affect CO_2 reduction activity.[55] Moreover, if DPs are not decomposed completely during charge, residuals accumulated on the cathode will

Table 1. Comparative summary of Li–CO$_2$ battery systems and the corresponding electrochemical performance.

DPs	Catalyst	Electrolyte	Discharge/charge potential (V vs Li/Li$^+$)	Coulombic efficiency [%]	Capacities	Rate	Stability	Refs.
Li$_2$CO$_3$ & C(Theoretical discharge voltage: 2.8 V)	RuO$_2$/NiO (active material-based electrodes)	1 M LiTFSI/TEGDME	1.1/— V	–	1.7 mAh cm^{-2} at 0.04 mA cm^{-2} (equal to 100 mA g^{-1})	–	–	[36]
	RuO$_2$/CNT (active material-based electrodes)	1 M LiTFSI/TEGDME	1.1/— V	–	1532 mAh g^{-1} at 100 mA g^{-1}	–	–	[36]
	CNT (active material-based electrodes)	1 M LiTFSI/TEGDME	1.0/— V	–	997 mAh g^{-1} at 100 mA g^{-1}	–	–	[36]
	CO$_2$–activated nitrogen-doped Graphene on reduced graphene oxide (active material-based electrodes)	1 M LiTFSI/TEGDME	2.2 /4.5 V	100	3000 mAh g^{-1} with a voltage limit of 4.5 V	Voltage gaps: 1.11, 1.38, 1.58, 1.74, 1.91, and 2.13 V at 50, 100, 200, 400, 800, and 1200 mA g^{-1}	A (small) increase in voltage gap of 0.12 V after 170 cycles at 500 mA g^{-1}	[37]
	2D single-atom-thick graphdiyne (integrated electrodes)	1 M LiTFSI/TEGDME	2.77 /4.17 V	–	18,416 mAh g^{-1} at 100 mA g^{-1}	Discharge/charge voltages: 2.37 /4.58 V at 800 mA g^{-1}; 2.33 /4.61 V at 1000 mA g^{-1}	158 cycles at 400 mA g^{-1} with curtailing capacity of 1000 mAh g^{-1}	[38]
	Topological defect-rich graphene (active material-based electrodes)	1 M LiTFSI + 0.3 M LiNO$_3$/TEGDME	2.8/4.25 V	90.80	69,000 mAh g^{-1} at 0.5 A g^{-1}	Voltage gap of 1.12 V at 100 mA g^{-1}; 1.87 V at 2.0 mA g^{-1}	600 cycles at 1.0 A g^{-1}	[39]
	Hierarchical Ti$_3$C$_2$T$_x$ MXene /carbon nanotubes (active material-based electrodes)	2 M LiTFSI/TEGDME	2.74 /4.15 V	96.8	11,458 mAh g^{-1} at 500 mA g^{-1}	Discharge voltage: 2.51 V at 2000 mA g^{-1}	After 100 cycles with terminal discharge /charge voltage: 2.58/4.38 V	[40]
	Covalent organic frameworks (COF) (active material-based electrodes)	1 M LiTFSI/TEGDME	2.1 /3.5 V	–	27,833 mAh g^{-1} at 75 mA g^{-1}	Overpotential: 1.08 V at 0.5 A g^{-1}	56 cycles with charge potential 3.5 V at 0.5 A g^{-1}	[41]

(Continued)

2210671 (9 of 33)

Table 1. (Continued).

DPs	Catalyst	Electrolyte	Discharge/charge potential (V vs Li/Li$^+$)	Coulombic efficiency [%]	Capacities	Rate	Stability	Refs.
Vertically aligned N-doped carbon nanotubes arrays (integrated electrodes)	Gel polymer electrolyte	2.4 /4.55 V	85.23	18,652 mAh g^{-1}	Potential gap to 1.96 V at 1000 mA g^{-1}	≈2520 h at 50 mA g^{-1} (63 cycles) and ≈2406 h at 500 mA g^{-1} (1203 cycles)	[42]	
Ru@Super P cathode (active material-based electrodes)	Molten $LiNO_3$/KNO_3	2.5 /3.2 V	93.6	Discharge /charge capacity: 5500 mAh g^{-1} at 5150 mAh g^{-1}	–	70 cycles with cut-off capacity of 1000 mAh g^{-1}	[43]	
Single-atom Ru implanted on Co_3O_4 nanosheets (active material-based electrodes)	1 M LiTFSI/TEGDME	2.5 /4.5 V	–	30, 915 mAh g^{-1} at 300 mA g^{-1}	–	251 cycles at 200 mA g^{-1}	[19a]	
Ru_{AC-SA}@NCB (active material-based electrodes)	1 M LiTFSI/TEGDME	2.58 /4.25 V	–	10, 651.9 mAh g^{-1} at 100 mA g^{-1}	Overpotentials: 1.65 and 1.86 V at 1 and 2 A g^{-1}	60 cycles at 300 mA g^{-1}	[44]	
Atomic Ir catalysts on Te substrates (integrated electrodes)	1 M $LiNO_3$/DMSO	2.5 /3.75 V	98.5	13, 247.1 mAh g^{-1} at 200 mA g^{-1}	Charge/discharge capacities of 13, 247/13, 441, 10, 282/10, 483, 7034/7333 and 5014/5359 mAh g^{-1} at 200, 1000, 1500 and 2000 mA g^{-1}	350 cycles with limited capacity of 500 mAh g^{-1}; 200 cycles at 1000 mA g^{-1}	[45]	

(Continued)

Table 1. (Continued).

DPs	Catalyst	Electrolyte	Discharge/charge potential (V vs Li/Li^+)	Coulombic efficiency [%]	Capacities	Rate	Stability	Refs.
Ir/carbon nanofibers (integrated electrodes)	1 M LiTFSI/TEGDME	2.76 /4.14 V	93.1	21,528 mAh g^{-1} at 50 mA g^{-1}	18,813 mAh g^{-1} at 100 mA g^{-1}	45 cycles at 50 mA g^{-1} with limited capacity of 1000 mAh g^{-1}		[46]
IrO_2/MnO_2–carbon-cloth (integrated electrodes)	1 M $LiClO_4$/TEGDME	2.5 /4.5 V	—	6604 mAh g^{-1} at 100 mA g^{-1}	1223 mAh g^{-1} at 800 mA g^{-1}	378 cycles at 400 mA g^{-1} with the limited capacity of 1000 mAh g^{-1}		[47]
W_2C nanoparticles embedded in carbon nanotubes (active material-based electrodes)	1 M $LiClO_4$/DMSO	3 /3.22 V	90.1	10,632 mAh g^{-1}	—	75 cycles at 200 mA g^{-1}		[20]
Single Co atoms anchored on graphene oxide (active material-based electrodes)	1 M LiTFSI/TEGDME	2.51 /4.15 V	82.5	17,358 mAh g^{-1} at 100 mA g^{-1}	—	>100 cycles at 100 mA g^{-1}		[48]
Freestanding MnOOH arrays (integrated electrodes)	1.0 M $LiCF_3SO_3$/TEGDME	2.8 /3.9 V	—	3000 mAh g^{-1} at 200 mA g^{-1}	—	138 cycles at a current density of 200 mA g^{-1} with limited capacity 1000 mAh g^{-1}		[18]
Sea urchin-like Mn_2O_3–Mn_3O_4 nanocomposite (active material-based electrodes)	1 M LiTFSI/TEGDME	2.75 /4.31 V	—	19,024 mAh g^{-1}	Charge potential 4.31 V at 800 mA g^{-1}; 4.04 V at 100 mA g^{-1}	1380 h at 100 mA g^{-1}		[49]

(Continued)

Table 1. (Continued).

DPs	Catalyst	Electrolyte	Discharge /charge potential (V vs Li/Li+)	Coulombic efficiency [%]	Capacities	Rate	Stability	Refs.
	Ni nanoparticles highly dispersed on N-doped graphene (Ni-NG) (active material-based electrodes)	1 M LiTFSI/TEGDME	2.5 /4.2 V	55.6	17, 625 mAh g^{-1}	Discharge platform: 2.82 V at 100 mA g^{-1}	100 cycles at cutoff capacity 1000 mAh g^{-1} at 100 mA g^{-1}	[50]
	NS_V-ReS_2 (5)/CP (active material-based electrodes)	1 M LiTFSI/TEGDME	2.88 /3.54 V	82.3	1811 µAh cm^{-2}	100 µAh cm^{-2}	Cycling for 700 h at 20 µA cm^{-2}, 350 h at 40 µA cm^{-2}, and 140 h at 100 µA cm^{-2},	[51]
	SACr@NG/PCF (active material-based electrodes)	1 M LiTFSI/TEGDME	2.8 /4.18 V	100	–	Voltage gap of 1.39 V at 100 µA cm^{-2}	>350 cycles with a voltage gap of 1.39 V at 100 µA cm^{-2}	[52]
$Li_2C_2O_4$ (theoretical discharge voltage:3.01 V)	Mo_2C/carbon nanotube Composites (active material-based electrodes)	1 M $LiCF_3SO_3$/TEGDME	2.8 /3.5 V	100	1150 mAh at 20 mA	–	40 cycles at 20 mA with controlled capacity 100 mAh	[13a]
	MoN nanofibers on carbon-cloth (integrated electrodes)	1 M LiTFSI/TEGDME	2.83 /3.19 V	88	6542.9 µAh cm^{-2}	Voltage gap of 0.36 V at 10 µA cm^{-2}, 0.94 V at 100 µA cm^{-2}	86 cycles at 100 µA cm^{-2} with curtailing the capacity of 100 µAh cm^{-2}	[23]
Li_2CO_3 & CO (theoretical discharge voltage:2.5 V)	Porous fractal Zn (integrated electrodes)	1 M LiTFSI/TEGDME	1.91 V/-	67	–	–	1500 min discharge	[25]
HCOOH (theoretical discharge voltage:2.8 V)	Nanoporous Pd films (active material-based electrodes)	1 M LiCl + 1 M HCOOLi/water	2.61 /2.87 V	91	–	Charge potential of 3.04 V at 1 mA cm^{-2}; 2.84 V at 0.1 mA cm^{-2}	300 h with charge potential 2.99 V	[13c]

**ADVANCED
SCIENCE NEWS**

www.advancedsciencenews.com

**ADVANCED
MATERIALS**

www.advmat.de

Table 2. Thermodynamic discharge potential for selected reaction and products.

Reaction	Product(s)	E^0 (V vs Li/Li$^+$)	Refs.
$4Li^+ + 4e^- + 3CO_2^- \rightarrow 2Li_2CO_3 + C$	Li_2CO_3 & C	2.80	[56]
$2CO_2 + O_2 + 4Li^+ + 4e^- \rightarrow 2Li_2CO_3$	Li_2CO_3	3.82	[57]
$4Li^+ + CO_2 + 4e^- \rightarrow 2Li_2O + C$	Li_2O & C	1.89	[16]
$2Li^+ + 2CO_2 + 2e^- \rightarrow Li_2C_2O_4$	$Li_2C_2O_4$	3.01	[13b]
$2Li + 2CO_2 + 2e^- \rightarrow Li_2CO_3 + CO$	Li_2CO_3 & CO	2.50	[25]
$2Li^+ + 3CO + 2e^- \rightarrow 2C + Li_2CO_3$	Li_2CO_3 & C	3.73	[58]
$CO_2 + 2H^+ + 2e^- + 2Li \rightarrow HCOOH + 2Li^+$	HCOOH	2.80	[13c]

gradually cover active sites and block Li$^+$ and CO$_2$. As a result, the significant effects on mass transfer and poor electrical conductivity will cause a gradual decrease of discharge potential and impacts will accumulate when cycling.

In recent years, the real operating voltage of Li–CO$_2$ batteries is questioned by some researchers. For example, Tan et al. report the real operating voltage, which is surprisingly found to be only 1.1 V in a Swagelok-type test device.[36] They demonstrated the CO$_2$ reduction reaction at the voltage of <2.0 V goes through the 4-electron reaction of $4Li^+ + 3CO_2 + 4e^- \rightarrow 2Li_2CO_3 + C$ based on findings from real-time TEM and galvanostatic intermittent titration technique. By decoupling small currents, 1% O$_2$, and 500 ppm H$_2$O, the operating voltage plateaus were improved to ≈2.0 V. Additionally, a high operating voltage of ≈2.6 V was achieved by a minor air leakage in test environment, confirming the impacts of the surrounding environment. However, the mechanisms of O$_2$ and/or H$_2$O participated discharge process are not fully revealed at present. Therefore, in depth investigation to identify related mechanisms is required to quantitatively determine the effects of surrounding environments in operating Li–CO$_2$ batteries. More in situ/operando characterizations, such as in situ Raman and differential electrochemical mass spectrometry (DEMS), are encouraged to track discharge products and intermediates on the cathode with the participation of O$_2$ and H$_2$O.

It is worth noting that several reported Li–CO$_2$ batteries in Table 1 achieve discharge potentials of higher than 2.8 V. For example, Zhang et al. report a high discharge potential of 3.0 V via employing the W$_2$C embedded CNTs in the system.[20] However, how can the discharge voltage be thermodynamically above the theoretical equilibrium potential of 2.8 V? What are the products in the case of these discharge voltages beyond the equilibrium potential? A major reason is the electric double layer formed on the carbon-based cathode surface that can provide extra capacity. Although this part of the capacity is not caused by the CO$_2$ reduction, the apparent discharge potential can be significantly elevated. That is why the N-doped ReS$_2$ catalysts with rich S vacancies (3N$_3$S$_V$-ReS$_2$) exhibit high discharge potential of 2.88 V.[51] This is evidenced in both Li–CO$_2$ and Li–O$_2$ batteries because carbon-based cathodes are widely employed in gas-involved batteries. One means to exclude this effect is to employ the non-carbon substrate for cathode preparation, for example, the Ni foam. Another reason is the change of reaction pathways and corresponding discharge products. For example, the formation of Li$_2$C$_2$O$_4$ product via $2Li^+ + 2CO_2 + 2e^- \rightarrow Li_2C_2O_4$ has a high theoretical equilibrium potential of 3.01 V.[23] If the catalysts can stabilize the Li$_2$C$_2$O$_4$ from the further conversion to Li$_2$CO$_3$ and

C, a high discharge voltage (>2.8 V) is likely exhibited. Cutting edge in situ/operando techniques such as in situ Raman are encouraged to confirm the formation of Li$_2$C$_2$O$_4$ as this product is not stable and can be readily decomposed to Li$_2$CO$_3$. Additionally, contaminates from the surrounding environments, such as O$_2$, may improve discharge potential and capacity via side reactions such as oxygen reduction via $O_2 + 4Li^+ + 4e^- \rightarrow 2Li_2O$ (theoretical equilibrium potential: 2.91 V). Therefore, it is important to exclude impurities in CO$_2$ gas and possible side reactions in order to clarify the real discharge potential.

3.1.2. Charge Potentials

As for charge potential in Li–CO$_2$ batteries, product properties and charge reactions are the primary factors. As discussed previously, discharge reactions in aprotic electrolyte mainly form Li$_2$CO$_3$ and C products. According to equilibrium potentials for each reaction summarized in **Table 3**, the solo decomposition of carbonate direct Li$_2$CO$_3$ decomposition is irreversible and occurs only at greater potential of >4 V, during which the O$_2$, or O$_2^-$ will also be generated as oxidation reaction product. However, when amorphous carbon participates in the charge reaction with the assistance of active catalysts, such as Ru, the charge potential can be significantly decreased through the concurrent decomposition reaction of Equation 1 with the thermodynamic charge potential of 2.8 V. Alternatively, the decomposition of other DPs, such as Li$_2$C$_2$O$_4$, Li$_2$CO$_3$ and CO and HCOOH, always correspond to lowered potentials because these products are not as stable as Li$_2$CO$_3$, and the decomposition is thermodynamically easier.

For a specific DP, properties including morphology, degree of crystallinity, and distribution are critical in affecting charge potential. Generally, Li$_2$CO$_3$ and C with smaller size, less crystallization, and "better" distribution correspond to lower charge overpotential. Wang et al. tuned properties of Li$_2$CO$_3$ and carbon by rational design of ZnS quantum dots /nitrogen-doped reduced graphene oxide (ZnS QDs /N-rGO) heterostructure.[59] Electronegative ZnS QDs are good at adsorbing CO$_2$ and transferring electrons, and providing more nucleation sites than that on the N-rGO. DP particles on ZnS QDs /N-rGO cathode grow faster in quantity, but slower in size, compared with that on N-rGO cathode. Benefiting from the good electronic transmission and high electrochemical activities of uniformly distributed ultrafine product particles at the interface, batteries with ZnS QDs /N-rGO cathode present a charge potential of 3.97 V at the current density of 200 mA g^{-1}, which is 0.48 V lower than that of N-rGO.

**ADVANCED
SCIENCE NEWS**

www.advancedsciencenews.com

**ADVANCED
MATERIALS**

www.advmat.de

Table 3. Thermodynamic charge potential for each reaction.

Reaction	Product(s)	E^0 (V vs Li/Li$^+$)	Refs.
$2Li_2CO_3 + C \rightarrow 4Li^+ + 4e^- + 3CO_2$	Li$^+$/CO$_2$	2.80	[16]
$2Li_2CO_3 \rightarrow 4Li^+ + 2CO_2 + O_2 + 4e^-$	Li$^+$/CO$_2$/O$_2$	3.82	[60]
$Li_2O \rightarrow 4Li^+ + O_2 + 4e^-$	Li$^+$ and O$_2$	2.91	[16]
$Li_2C_2O_4 \rightarrow 2Li^+ + 2CO_2 + 2e^-$	Li$^+$/CO$_2$	3.01	[13d]
$Li_2CO_3 + CO \rightarrow 2Li^+ + 2CO_2 + 2e^-$	Li$^+$/CO$_2$	2.50	[25]
$HCOOH + 2Li^+ \rightarrow CO_2 + 2H^+ + 2e^- + 2Li^+$	Li$^+$/CO$_2$/H$^+$	2.80	[13c]

Additionally, tuning the crystallinity of DPs from crystalline to amorphous decreases the charge potential because Li_2CO_3 with lower degree of crystallinity decomposes relatively readily. Mao et al. reported that a functional electrocatalyst composed of ultra-fine IrO_2 particles and thin-layered δ-MnO_2 sheets (IrO_2/MnO_2) favors the formation of DPs with a less crystalline feature.[47] IrO_2 possibly acts as the catalytically active center for the nucleation and growth of DPs because of the high catalytic activity of ultra-fine IrO_2 particles. The synergistic catalytic effect of MnO_2 sheets with abundant catalytic sites provides sufficient nucleation sites and leads to the conformal growth of thin-layered Li_2CO_3. This Li_2CO_3 structure can be readily decomposed at a lower potential of 4 V at the current density of 100 mA g^{-1}.

3.2. Battery Capacity Affected by DPs

The capacity of a Li–CO$_2$ battery measures the maximum amount of energy that can be extracted from the battery during CRR or CER. It is generally acknowledged that the battery capacity of Li–CO$_2$ batteries is closely related to accumulated DPs that are deposited on the cathode surface, or within cathode structures.

The initial porosity of the cathode is the determining factor to the battery capacity. Rich channels and pores favor the mass transportation of Li$^+$ and CO$_2$ and provide large spaces for DP decomposition.[61] Li et al. compared the performance of $MnCO_3$, $Mn(HCOO)_2$, $Mn_2(dobdc)$ (dobdc = 2,5-dioxido-1,4-benzenedicarboxylate) with different crystal structures. They found the $Mn_2(dobdc)$ MOF structure with the large pore size of $\approx$11 Å and high CO$_2$ uptake of 143 cm^3 g^{-1} (at 1atm and 298 K) can reach a full capacity of 18, 022 mA g^{-1}.[41] By contrast, the non-porous $MnCO_3$ with near zero CO$_2$ uptakes can only reach $\approx$11, 000 mA g^{-1}. Moreover, the type of porosity also plays a significant role in battery capacity. Generally, on a cathode with uniform porosity, both the gas side and the electrolyte side with saturated CO$_2$ have short CO$_2$ transport route and DPs tend to accumulate near two edges.[62] The internal transport channels are obstructed with less in the center of cathode, leading to the low utilization of the void volume and a low discharge capacity. Therefore, it is ideal to set large porosity at both side of the cathode to accelerate mass transport and avoid the obstruction. The internal of the cathode should have small porosity to enhance the mechanical strength. To reach this goal, it is worthy to explore cathode designs with continuous gradient porosity for large DP accumulation.

The battery capacity is closely related to charge/discharge rate, for example, Xiao et al. displayed the discharge–voltage curves at various current densities on a CNT-based cathode and found the full capacity at 0.2 mA cm^{-2} (4881.03 mAh g^{-1}) was 35.2% higher than that at 0.5 mA cm^{-2} (3611.83 mAh g^{-1}).[62] They identified, based on SEM results, that the DP morphology evolves significantly from small particles to large Li_2CO_3 crystals with an increase of current density. Therefore, they attributed the capacity discrepancy at various current densities to morphology differences in DPs. By theoretical simulation, they identified that large plate-like DPs show limited full capacities, while the needle-like ones could reach high capacities, a result that further identified the relationship between current density/DP morphology/capacities. Therefore, the discharge/charge rate is one of the significant factors related to the morphology of deposited DPs and corresponding changes in capacity.

Moreover, the DP structure and corresponding growth mechanism have a significant impact on battery capacity because the solid Li_2CO_3 product is an insulator. The deposition on the surface gives rise to electronic resistance and isolates the contact of reactants and catalysts. If DPs grow through the surface adsorption growth mechanisms, a conformal insulating film will be formed at the surface of the catalyst, resulting in surface passivation and lower maximum capacity. However, if DPs grow through the solvation-mediated growth mechanism, more flower-like Li_2CO_3 will assemble on the cathode surface. In this instance, active sites are covered less by-products, and increased product accommodation spaces can be efficiently used.

3.3. Battery Stability Affected by DPs

Battery stability is critical in Li–CO$_2$ batteries, and instability significantly affects overall performance, including round-trip efficiency, cycling performance, and safety. It generally involves the chemical stability of electrode materials and interfaces, the electrochemical stability of cell during charge /discharge, and mechanical stability in variations of external or internal stress. Amongst them, the deposition behavior of commonly used Li anodes, and electrochemical performance have been widely reported in Li ion or L–O$_2$ battery-related studies.[63] In this section, the significant impacts of DPs on the stability of cathode structure and the related electrochemistry will be emphasized.

As one of the main DPs, Li_2CO_3 is a solid-state insulator that requires high potential for electrochemical decomposition. When incomplete decomposition of Li_2CO_3 and C occurs, residual Li_2CO_3 will gradually stack on the cathode and form insulating barriers, leading to increased impedance and high charge overpotential. This accelerates cycling decay with inferior

ADVANCED
SCIENCE NEWS

www.advancedsciencenews.com

ADVANCED
MATERIALS

www.advmat.de

Coulombic efficiencies. Meanwhile, the structure of Li_2CO_3 is critical in determining deposition. For example, when inhomogeneous bulk Li_2CO_3 accumulates to a particular thickness on discharge, the formed dense passivation layer will result in substantial decomposition difficulty during charge. The high charge overpotential inevitably induces decay of electrolytes and electrodes, resulting in decreased cycle life.[64] This phenomenon can be further extended to other solid DPs in Li–CO_2 batteries such as $Li_2C_2O_4$.

Parasitic side reactions and corresponding by-products such as superoxide anion, $O_2^{\bullet-}$, generated at the interface of cathode and electrolyte, especially at high overpotentials, can affect the battery stability.[55,65] Decomposition of Li_2CO_3 is one of the main route for $O_2^{\bullet-}$ generation (Equation 9), which occurs at high charge overpotential without the participation of C. Another route for $O_2^{\bullet-}$ generation is the participation of O_2 in CO_2 reduction. In O_2-involved Li–CO_2 batteries, the oxygen reduction reaction to form $O_2^{\bullet-}$ species is the thermodynamically favored process (Equation 17) as the direct reduction of CO_2 molecules requires a highly negative potential. $O_2^{\bullet-}$ radicals with strong oxidizing properties could react with electrolyte solvents such as DMSO and TEGDME, resulting in energy loss and more complex new radicals and by-products.[66] Meanwhile, gas diffusion electrodes, including catalysts, carbon-based support, and the binder, can also be eroded, which accelerates deterioration in battery performance.[67]

$CO_4^{\bullet-}$ is another by-product generated in the $O_2^{\bullet-}$-involved system. The $O_2^{\bullet-}$, acting as a strong nucleophilic free radical, can attack the carbonyl carbon in CO_2 by Equation 18 and form the intermediate, $CO_4^{\bullet-}$. Normally, this radical tends to react with CO_2 to form $C_2O_6^{\bullet-}$ (Equation 19). The $C_2O_6^{\bullet-}$ can then be attacked by active $O_2^{\bullet-}$ radicals to form $C_2O_6^{2-}$ and O_2 via Equation 20. After that, the $C_2O_6^{2-}$ can react with another two $O_2^{\bullet-}$ radicals to form Li_2CO_3 and O_2 through Equation 21. Here, the $CO_4^{\bullet-}$ acts as an intermediate to transfer electrons and form the solo discharge products, Li_2CO_3. When in DMSO-based electrolyte, the $CO_4^{\bullet-}$ tends to react with Li^+ to form $LiCO_4$, followed by the reaction with Li^+, CO_2, and electrons, to form Li_2CO_3 through Equations 22 and 23. In $CO_4^{\bullet-}$-involved reaction pathways, the overall reaction during discharge can be written as Equation 24. During charge, the solo decomposition of Li_2CO_3 requires higher charge potential (>4.5 V) compared with the concurrent decomposition, resulting in the degradation of catalysts and electrolytes. Therefore, in the $CO_4^{\bullet-}$-involved reaction pathways, DPs change from Li_2CO_3 and C to Li_2CO_3 product, resulting in large charge overpotential and deteriorating battery stability.

$$O_2 + e^- \leftrightarrow O_2^{\cdot-} \tag{17}$$

$$O_2^{\cdot-} + CO_2 \leftrightarrow CO_4^{\cdot-} \tag{18}$$

$$CO_4^{\cdot-} + CO_2 \leftrightarrow C_2O_6^{\cdot-} \tag{19}$$

$$C_2O_6^{\cdot-} + O_2^{\cdot-} \leftrightarrow C_2O_6^{2-} + O_2 \tag{20}$$

$$C_2O_6^{2-} + 2O_2^{\cdot-} + 4Li^+ \leftrightarrow 2Li_2CO_3 + 2O_2 \tag{21}$$

$$CO_4^{\cdot-} + Li^+ \rightarrow LiCO_4 \tag{22}$$

$$LiCO_4 + 4Li^+ + CO_2 + e \leftrightarrow 2Li_2CO_3 \tag{23}$$

$$4Li + 2CO_2 + O_2 \leftrightarrow 2Li_2CO_3 \tag{24}$$
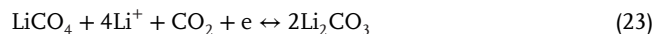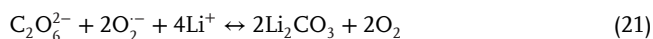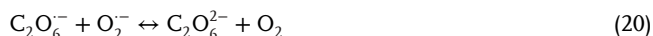
This review focuses however on aprotic Li–CO_2 batteries, while battery stabilities in aqueous Li–CO_2 batteries are less reviewed. If Li metal is used however in aqueous Li–CO_2 batteries, the safety issue and rapid chemical reactions between Li metal and aqueous electrolytes should be the most important factor that needs to be addressed first. It is concluded that the performance of Li–CO_2 batteries is significantly impacted by physicochemical properties of DPs. Although the development of efficient catalysts and electrolyte is helpful for improvement of performance, what they did is to essentially regulate the properties of DPs and boost their decomposition during charge. It is necessary however to deepen present understanding of the influencing mechanism of related DPs to design highly reversible practical, aprotic Li–CO_2 batteries.

It is worth noting that both "mA g^{-1}" and "mA cm^{-2}" can be used as the unit of current density in Li–CO_2 batteries (**Table 1**). "mA cm^{-2}" reflects the amount of charge that flows through a unit area of a chosen cross section. It is particularly meaningful for the performance assessment of planar electrodes or electrodes with defined surface area. Compared with "mA cm^{-2}," "mA g^{-1}" focuses more on the electrochemical properties of powder materials loaded on the substrates. It refers to the current density normalized by the mass of the active materials on the electrode. This unit is widely used when comparing the performance of materials with high surface area, such as porous or nanostructured materials. In Li–CO_2 batteries, the catalyst materials loaded on cathodes usually have rich pores and channels, which makes it difficult to define the surface area. Thus, "mA cm^{-2}" is not suitable for these porous catalyst-based Li–CO_2 batteries. In addition, rsearchers find the battery performance is closely related to the loading of catalysts. Thus, a majority of literatures prefers the use of "mA g^{-1}" in Li–CO_2 batteries. Moreover, standardization of current density unit is significant for performance evaluation and comparison of results reported in different studies. Therefore, it is strongly recommended to standardize the current density unit to "mA g^{-1}" in future studies in Li–CO_2 batteries.

4. Characterizations for DPs in Li–CO_2 Batteries

An improved understanding of DPs and related reaction mechanisms is of significance for the design of high-performance Li–CO_2 batteries. Thanks to the development of advanced techniques, progress has been made in characterizing DPs and reveal the formation /decomposition mechanism(s). In this section, we will focus on techniques of ex situ, in situ, and operando measurements in revealing fundamental insights into the formation/decomposition mechanism of DPs.

4.1. Ex Situ measurements

Ex situ techniques provide significant information about the properties of DPs and can be used to evidence interaction(s) with

2210671 (15 of 33)

**ADVANCED
SCIENCE NEWS**

www.advancedsciencenews.com

**ADVANCED
MATERIALS**

www.advmat.de

catalysts, or electrolytes. By disassembling the cathode from batteries at varied discharging of depth (DOD), or status of charging (SOC), formation /decomposition mechanism(s) for DPs can be determined. Specifically, the morphology change of DPs after discharge and charge can be identified by microscopy techniques, including scanning electron microscopy (SEM), transmission electron microscopy (TEM), and scanning transmission electron microscopy (STEM).[3a,c,52] Emerging cryo-SEM and cryo-TEM are demonstrated to be especially useful in imaging of three-phase interface in cathodes.[68] A highly sensitive surface topography makes electron microscopies, more or less, ideal for surface investigation, especially for DPs composed of Li_2CO_3, Li_2O, C, and $Li_2C_2O_4$. Importantly, integrated energy-dispersive spectroscopy (EDS) and electron energy loss spectroscopy (EELS) modules provide detailed structural information for electrodes and distinguish elemental distribution and composition in DPs.[69]

Powder diffraction is a rapid analytical technique using X-ray diffraction (XRD), neutron power diffraction (NPD), or electron powder diffraction (EPD), for the identification of the structure of unknown crystalline phase and to provide information in one unit cell dimensions.[70] These facilities are critical in Li–CO_2 batteries to identify DPs and decomposition products, together with by-products including Li_2O and Li_2O_2.[45] Via monitoring products after charge, XRD helps identify whether products accumulate, which is critical to solve problems of poor cycling. Because both the surface and interface of electrodes can affect the electrochemical performance, surface-sensitive spectroscopic techniques, including Raman spectroscopy, Fourier transform infrared spectroscopy (FT-IR), and X-ray photoelectron spectroscopy (XPS) need to be used.[3a,71] XPS, a quantitative technique, provides information about oxidation states, the composition of DPs /by-products, together with the interaction with cathode and electrolyte.[72] Raman and FT-IR can be employed to identify surface species, especially amorphous discharge products.[9b,73] Significantly, although a contamination-free sample is necessary for ex situ characterization, environmentally sensitive electrodes are inevitably contaminated by air or moisture during sample transfer /loading, resulting in uncertainty in measurement. Nevertheless, by characteristics of disassembled batteries disrupted at different cycling state, these techniques do provide plenty of reliable information about DPs in Li–CO_2 batteries.

4.2. In Situ/Operando Techniques

DP formation and decomposition involve complex reactions and intermediates during cycling. Because ex situ characterization techniques for disassembled batteries are destructive, they cannot be used to identify unstable and metastable intermediates.

In contrast to ex situ techniques, in situ instruments allow characterization without disassembly, and therefore provide more realistic information about discharge /charge products and mechanism(s). Operando characterization permits real-time monitoring of product states and changes in discharge /charge reactions. Here, we review the application of in situ /operando techniques in identifying intermediates, monitoring the formation /decomposition of DPs, and determining the interaction between catalysts and products at the interface. Both qualitative and quantitative analysis techniques in **Figure 7** are critically assessed in the analysis of mechanisms.

4.2.1. In Situ Qualitative Analysis: Raman, RRDE, EPR, UV–Vis, and SEM

Raman spectroscopy is an important spectroscopic technique based on the vibrational characteristic effects of the incident laser beam on inelastic scattering.[74] It is widely used to observe vibrational transitions in homopolar bindings, including C–C bonds and O–O bonds, where the infrared transition is not active.[75] At present, via metal surface plasmonic resonance, in situ surface-enhanced Raman spectroscopy (SERS) is established based on Raman theory.[76] With enhanced Raman scatting of as high as 10^{14} times, in situ SERS is a practically powerful technique to identify the underlying chemical state change and intermediate species in Li–CO_2 batteries.[38,77] Because of the surface-enhanced effect of gold sputtered on cathode, in situ SERS provides "rich" spectrum information on intermediates including Li_2O, carbon species, oxalate species ($C_2O_4^{2-}$), CO, and Li_2CO_3, which is critical to speculate and provides insights into reaction mechanism(s).[53,78] For example, Qiao et al. explored discharge/charge mechanisms using in situ SERS (**Figure 8**a,b).[16] At the capacity of 10 µAh, Raman peaks appearing at 1085, 1319, and 1587 cm^{-1} can be assigned to specific vibration modes in Li_2CO_3 and the D/G band in carbon (**Figure 8**c–f). These peaks gradually grew during discharge with a synchronously increasing trend. However, when the discharge capacity was extended to 20 µAh, a new plateau was exhibited at 1.8 V. A new peak of Li_2O at 520 cm^{-1} gradually appeared whilst the accumulation of Li_2CO_3 did not increase after 10 µAh. This directly evidenced that the formation mechanism for Li_2CO_3 is affected by mass transport. Benefiting from the in situ SERS, they also found direct evidence for the Li–CO_2 battery transition from irreversible on Au cathode to reversible on a Ru cathode. On a Ru cathode during charge, the Li_2CO_3 and C species peaks decreased concurrently, and the Raman peak intensity reached the minimum at ca. 3.6 V. However, only the peak for Li_2CO_3 exhibited a significant decreasing trend at the charge voltage of 4.05 V. The unchanged peaks of G-band species confirm irreversible reactions on Au-based cathode, and successful fixation of CO_2 into C species.

The discharge /charge mechanism can be analyzed from the appearance of intermediates and the related order of appearance in the in situ SERS spectra. Most recently, Zhao et al. used in situ SERS spectroscopy to investigate CO_2 reduction on $Cu_{ML}@Au$ electrocatalysts in CO_2 saturated DMSO-based electrolyte (**Figure 9**).[26] When scanning the potential from OCV to 2.5 V, they detected the G band of carbon. However, the D band of carbon (1360 cm^{-1}) and the $C_2O_4^{2-}$ intermediate (1489 cm^{-1}) for the formation of C species did not appear (**Figure 9**a). Therefore, the reaction of $4Li^+ + 3CO_2 + 4e^- \rightarrow 2Li_2CO_3 + C$ in $Cu_{ML}@Au$ can be ruled-out. Additionally, they detected the Raman peak of CO at 2135 cm^{-1} but failed to observe the concurrent appearance of CO_3^{2-} and CO, together with Li_2O species at 521 cm^{-1}. Therefore, they proposed the CO_2RR mechanism presented in Equations 25 and 26. Furthermore, in situ SERS spectra are also used to determine electrolyte influence on CO_2 reduction.

ADVANCED
SCIENCE NEWS

www.advancedsciencenews.com

ADVANCED
MATERIALS

www.advmat.de
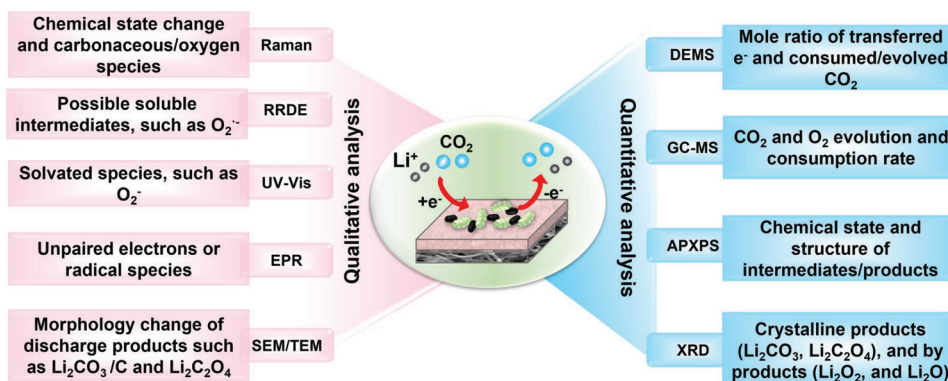
Figure 7. In situ /operando characterizations and application in Li–CO$_2$ batteries.
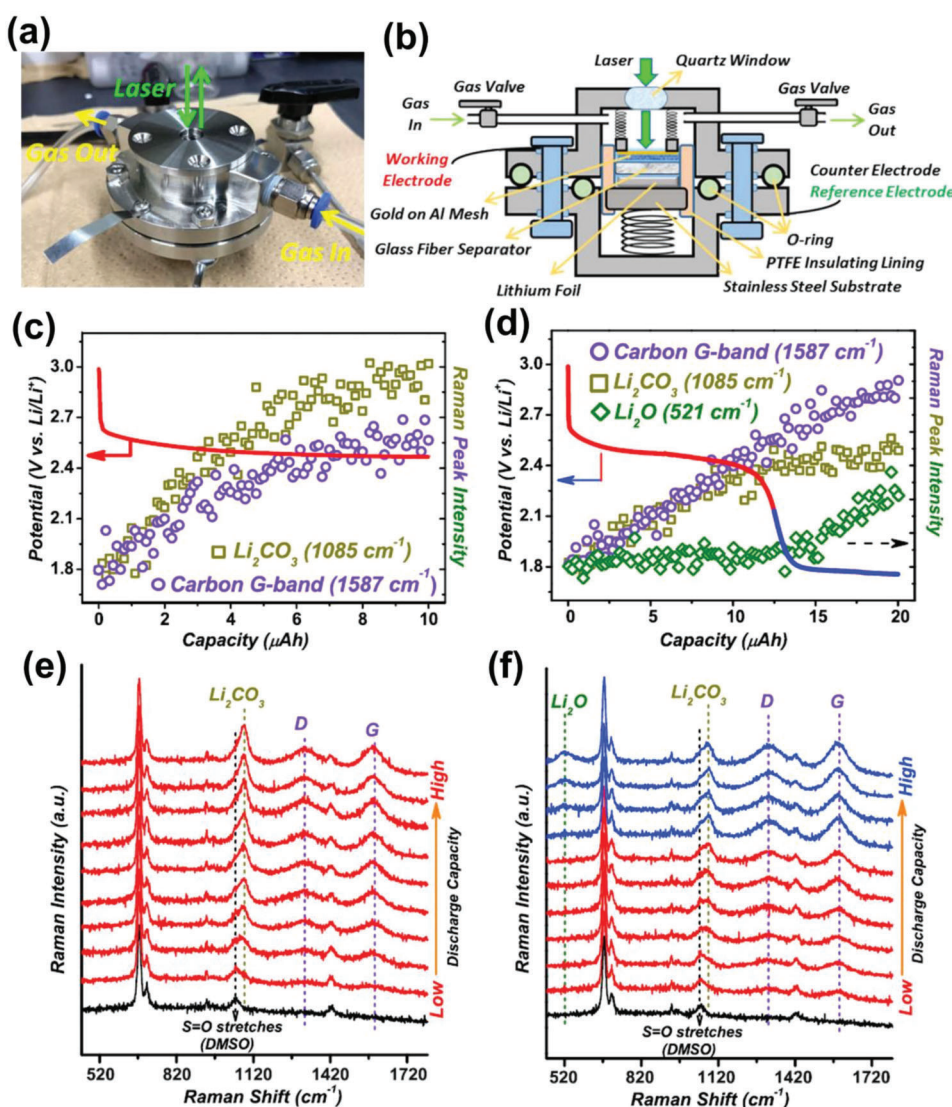
Figure 8. Applications of in situ SERS to Li–CO$_2$ batteries on Ru catalyst. a) Photograph and b) schematic illustration of in situ SERS cell for Li–CO$_2$ batteries. Galvanostatic discharge profiles with a capacity limit of c) 10 μAh and d) 20 μAh, at the current density of 5 μA. e,f) Capacity-dependent in situ SERS during corresponding discharge in (c) and (d). Reproduced with permission.[16] Copyright 2017, Elsevier.

2210671 (17 of 33)
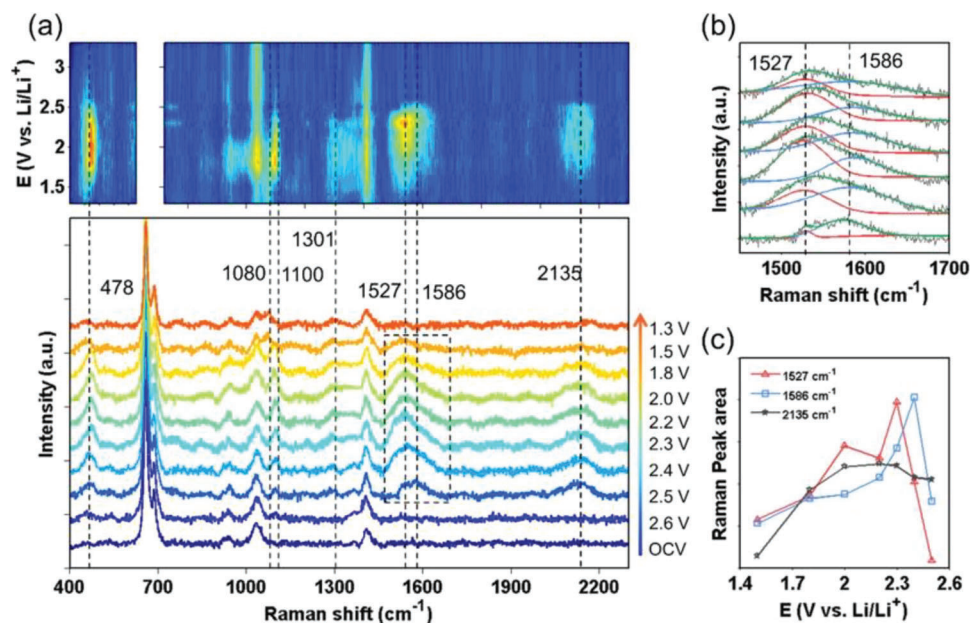
Figure 9. Applications of in situ SERS to Li–CO_2 batteries for Cu_{ML}@Au electrocatalysts. a) Raman intensity as a function of potential in CO_2 saturated 0.1 M $LiClO_4$–DMSO electrolyte. Peaks at 1301, 1527, and 1586 cm^{-1} are attributed to the stretching vibration of C–O band in CO_2^- anion. The peak at 2135 cm^{-1} appearing at 2.5 V is assigned to CO. b) Magnified spectral profile of the outlined region of (a). c) Profile for Raman peak areas at 1527, 1586, and 2135 cm^{-1} as a function of potential. Reproduced with permission.[26] Copyright 2022, American Chemical Society.

In Cu_{ML}@Au system, Raman peak area of OC*O*$^-$ adsorption mode at 1586 cm^{-1} and CO at 2135 cm^{-1} are mainly correlated. When Li^+ was replaced with TBA^+ in the electrolyte, the dominant OC*O*$^-$ became coexistent with OC*O$^-$ and OC*O*$^-$ and the CO peak was reduced compared with that in Li^+ electrolyte, demonstrating the promotion of Li^+ in the conversion of CO_2^- to CO.

$$LiCO_2 + CO \rightarrow LiCO_3 + CO \quad (25)$$

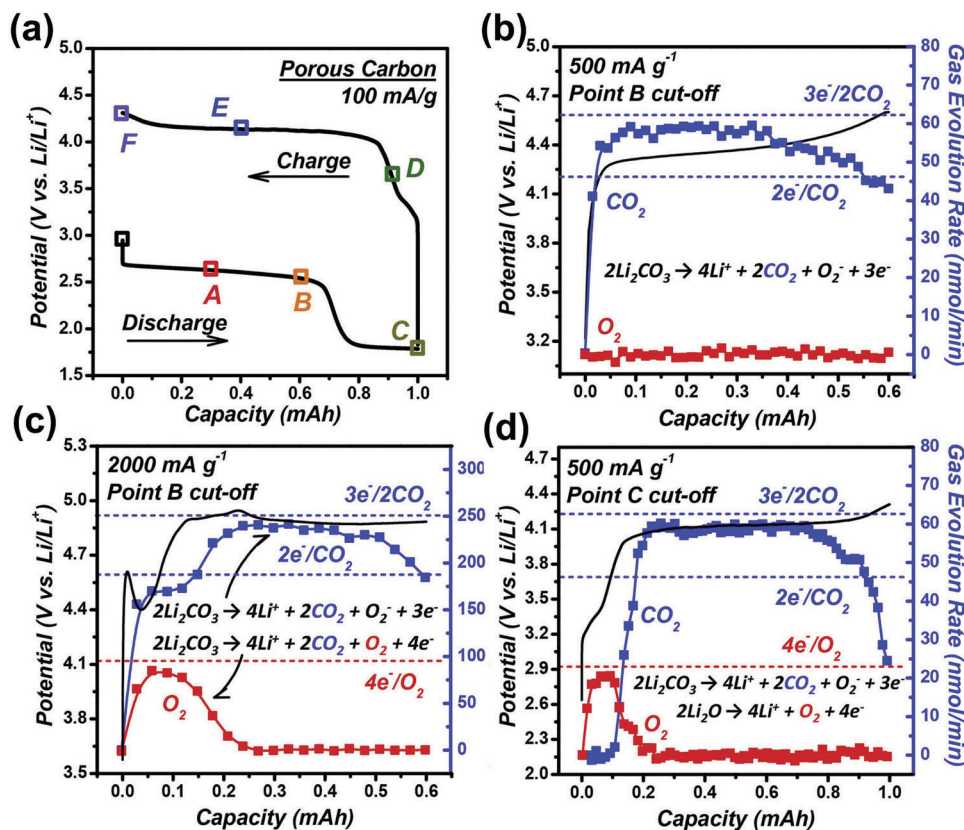$$LiCO_3 + e^- + Li^+ \rightarrow Li_2CO_3 \quad (26)$$

Overall, in situ SERS is a "good" qualitative technique to probe where/when/how DPs or intermediates accumulate and decompose via the display of changes in peak intensities and corresponding locations. However, there are several limitations that existed with in situ SERS during characterization of Li–CO_2 batteries. For example, SERS is only sensitive in proximity to the surface of the specimen and not all vibrational modes of DPs, intermediates, and solvents produced in Li–CO_2 batteries are Raman active, possibly resulting in incomplete information about DPs. In addition, usually invisible Raman peak at particular vibration modes can be detected as a result of strong electric field gradient, confusing the following analyzes of the data obtained. To a certain extent, in situ SERS results therefore should be confirmed with other characterization methods and theoretical computations.

In addition, to confirm possible soluble intermediates, such as $O_2^{\cdot-}$ and $Li_2C_2O_4$, rotating ring-disk electrode (RRDS) has been used to assess Li–CO_2 batteries.[5a,79] Although, at present, RRDS is not widely used in Li–CO_2 battery studies, this may be effective to explore the electrochemical decomposition mechanism of

Li_2CO_3. In situ ultraviolet–visible (UV–vis) spectroscopy can be used to monitor solvated species, such as $O_2^{\cdot-}$ (at around 252 nm). Operando electron paramagnetic resonance (EPR) spectroscopy is another technique to assess paramagnetic molecules.[80] In Li–CO_2 batteries, it can be used to detect unpaired electrons generated in discharge /charge and radical oxygen species. To monitor the nucleation /growth and decomposition of DPs, in situ SEM or TEM can be used for determining morphology. Thus, possible reaction mechanisms can be identified.

4.2.2. In Situ Quantitative Analysis: DEMS, GC-MS, APXPS, and XRD

Compared with qualitative analysis, the quantitative analysis provides potentially stronger evidence for analyses of mechanisms as it is more accurate and convincing. These techniques can not only benefit the prediction of mechanisms, but also help rule out the unreasonable speculation. Specifically, the differential electrochemical mass spectrometry (DEMS) offers quantitative data through a combination of electrochemical experimentation with mass spectrometry.[81] By DEMS, the mole ratio of the electron transfer number and consumption, together with the evolution rates of CO_2 and O_2 molecules can be determined. Advantages of this technique are the high test speed and sensitivity (amounts below 1 nmol).[82] Qiao et al. applied in situ DEMS to distinguish possible charge mechanisms as shown in **Figure 10**.[16] DEMS findings in **Figure** 10b evidence the evolution of CO_2 with negligible O_2 when the discharge stops at point-B at the current density of 500 mA g^{-1} (**Figure 10a**). The related charge-to-mass ratio for CO_2 is nearly $3e^-/2CO_2$, demonstrating the solo decomposition of Li_2CO_3 (Equation 9: $2Li_2CO_3 \rightarrow 4Li^+ + 2CO_2 + O_2^{\cdot-} + 3e^-$).

ADVANCED
SCIENCE NEWS
www.advancedsciencenews.com
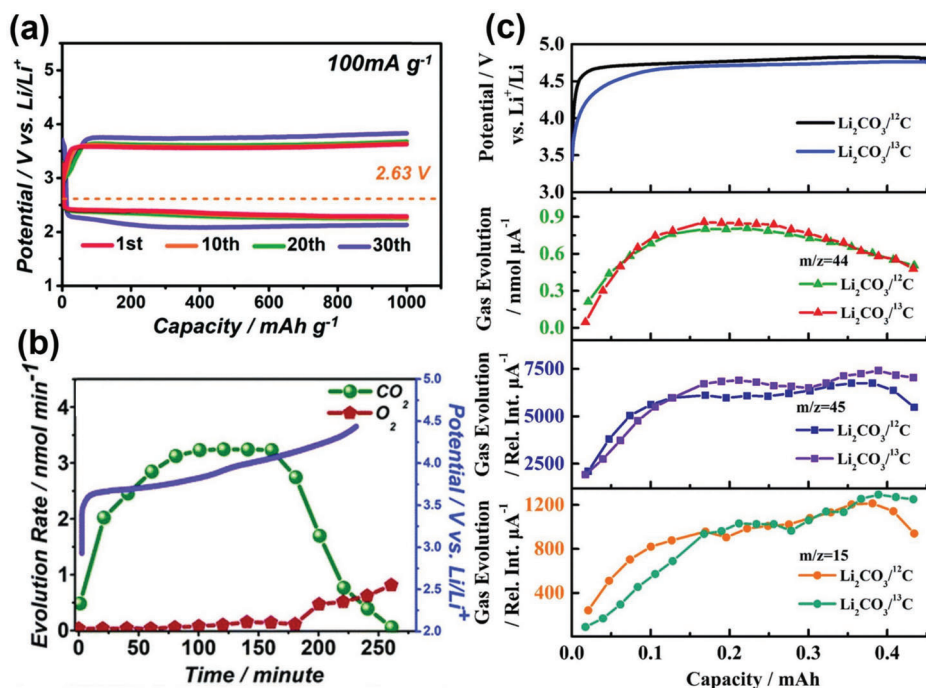
**ADVANCED
MATERIALS**
www.advmat.de

Figure 10. Application of DEMS to quantitatively determine mechanisms of Li–CO$_2$ batteries. a) Voltage profile of a Li–CO$_2$ battery with charge cutoff 4.5 V and discharge capacity 10.0 mAh at 100 mA g^{-1}. DEMS findings for gas evolution rates for CO$_2$ and O$_2$ during charge after discharged to point B at b) 500 mA g^{-1} and c) 2000 mA g^{-1} and point C at d) 500 mA g^{-1}. Reproduced with permission.[16] Copyright 2017, Elsevier.

When the current density is increased to 2000 mA g^{-1}, a peak of O$_2$ appears at the early state of charge in **Figure 10c**. The charge-to-mass ratio of 4e$^-$/O$_2$ confirms the charge reaction of 2Li$_2$CO$_3$ → 4Li$^+$ + 2CO$_2$ + O$_2$ + 4e$^-$. When discharge capacity is extended to point-C in **Figure 10a**, the O$_2$ species is also observed at lower potential at the initial stage of subsequent charge in **Figure 10d**. The proposed decomposition mechanism is 2Li$_2$O → O$_2$ + 4Li$^+$ + 4e$^-$. Meanwhile, Lian et al. proposed a new catalyst consisting of Ru single atoms and a Co$_3$O$_4$ nanosheet array grown on carbon cloth (SA Ru-Co$_3$O$_4$/CC) with boosted electrochemical performance, including, low overpotential, ultrahigh capacity, and long cycle life.[19a] To investigate the operating mechanism for Li–CO$_2$ batteries, in situ DEMS was used to monitor the consumption and production rate of CO$_2$ under the current density of 0.2 mA with a cutoff capacity of 0.2 mAh.[19a] According to the generally accepted discharge and charge reactions in reversible Li–CO$_2$ batteries, the theoretical molar ratio of electron transfer to CO$_2$ generation and consumption is about 1.33 (charge-to-mass ratio, e$^-$/CO$_2$), based on a four-electron transfer process. Experimental results demonstrate that the e$^-$/CO$_2$ ratios in cathode containing SA Ru-Co$_3$O$_4$/CC catalyst are 1.37 and 1.39 for discharge and charge, respectively, which are close to the theoretical values. That is, when applying SA Ru-Co$_3$O$_4$/CC catalysts, the battery discharge and charge mechanisms follow Equations 1 and 11, respectively, with Li$_2$CO$_3$ and C as the main DPs. In this way, the reaction can be easily distinguished by in situ DEMS re-sults controlled within a margin of error. However, only volatile products or intermediates are detectable via in situ DEMS. Other species in liquid or solid states that consume electrons cannot be detected in this way. Therefore, in situ DEMS test is powerful when only gaseous species consume electrons in involved reactions.

Gas chromatography-mass spectrometry (GC-MS) is another hybrid analytical technique that combines separation capabilities of GC with the detection properties of MS to efficiently provide data for analyses.[83] In Li–CO$_2$ batteries, GC-MS offers real-time and on-line quantitative analysis with reliability for detecting rates of CO$_2$ and O$_2$ evolution and consumption during battery operation. Wang et al. used in situ GC-MS measurements to monitor gases formed on a super P-based cathode in molten salt Li–CO$_2$ batteries as is shown in **Figure 11**a,b.[43] The detected CO$_2$ gas confirmed the decomposition of Li$_2$CO$_3$ and battery reversibility. A small amount of O$_2$ detected at the end of charge confirmed the electrochemical decomposition of electrolyte when the potential reached 4.2 V. Yang et al. assessed the charge mechanism for Li–CO$_2$ batteries by coupling in situ GC-MS and isotopic tracing.[84] **Figure 11**c presents the charge profiles for Li$_2$CO$_3$-covered electrodes in two cells using ^{12}C and ^{13}C carbon as conductive additives. In this system, three GC-MS fragments, $m/z = 44$, $m/z = 45$, and $m/z = 15$ appeared and decreased after charge. Because no O$_2$ was detected throughout the charge, the O$_2$ evolution reaction (Li$_2$CO$_3$ → CO$_2$ + 1/2O$_2$ + 2Li$^+$ + 2e$^-$)

**ADVANCED
SCIENCE NEWS**

www.advancedsciencenews.com

**ADVANCED
MATERIALS**

www.advmat.de

Figure 11. Application of GC-MS to quantitatively determine mechanisms of Li–CO₂ batteries. a) Cycling stability of super P in Li–CO₂ cells in LiNO₃/KNO₃ molten nitrate electrolyte at the current density of 100 mA g⁻¹. b) CO₂ and O₂ evolution rates during charge in molten salt Li–CO₂ batteries via in situ GC-MS. Reproduced with permission.[43] Copyright 2021, Royal Society of Chemistry. c) Charge profile of electrode pre-filled by Li₂CO₃ with ¹²C or ¹³C carbon as conductive additive at 36 mA g⁻¹ and gas evolution rate for fragment-44, 45, and 15. Adapted with permission.[84] Copyright 2016, Royal Society of Chemistry.

is not valid for Li_2CO_3 decomposition. The $^{12}CO_2$ in the two cells was nearly equal as the gas evolution of m/z = 44 fragments have similar readings at each capacity. In addition, if the charge undergoes concurrent decomposition of Li_2CO_3 and C, the cell using ^{13}C as a conductive additive generates 1/3 less $^{12}CO_2$ than the cell using ^{12}C. Therefore, the mechanism for $Li_2CO_3 + 1/2C \rightarrow 2Li^+ + 3/2CO_2 + 2e^-$ can also be ruled out in this Li–CO₂ system. The authors attributed fragments m/z = 45 and m/z = 15 to the gas from the electrolyte decomposition because of the oxidizing properties of O_2^{-} from mechanism for $Li_2CO_3 \rightarrow CO_2 + 2Li^+ + O_2^{-}$. However, only thermally stable volatility can be detected by GC-MS. Moreover, sample degradation induced by the GC injector, columen, or ion source can also lead to misleading information. Therefore, characterization results from other techniques including, FTIR and Raman need to be combined to qualitatively analyze reactions and confirm gaseous components before quantitative analysis via GC-MS.

As an emerging surface-sensitive technology, in situ ambient-pressure X-ray photoelectron spectroscopy (APXPS) is also a useful technique to assess surface chemistry of cathodes, DPs, and intermediates, together with variation during charge and discharge. With advances in APXPS hardware, synchrotron capabilities, and increased brightness of laboratory X-ray sources, time-resolution across multiple-length scales has improved to sub-nanosecond.[85] Especially, with a synchrotron source, the excitation energy can be selected for nondestructive depth profiling, which gives more reliable information for in situ analysis. Wang et al. used the synchrotron-based in situ APXPS (**Figure 12**)

to assess real-time Li–CO₂ reaction chemistry in ionic liquid electrolyte.[86] The authors demonstrated that pure CO₂ reduction is electrochemically inert on porous carbon electrode at room temperature and that the kinetics is highly significantly improved by H_2O. They assessed CRR under three different gas components at 5 mbar (ca. pure CO₂, CO_2/H_2O, and CO_2/O_2), on a porous carbon surface with ionic liquid (0.5 M LiTFSI in 1-butyl-1-methyl-pyrrolidinium bis(trifluoromethylsulfonyl)imide (Pyr₁₄TFSI)). This ionic liquid was selected to facilitate CO₂ capture and stabilize CRR intermediate anions because of its strong solvation for Li^+. According to XPS results obtained upon discharge in pure CO₂, no new peak was observed on carbon electrode during the entire discharge, confirming that no new species was formed. In comparison, the C 1s, O 1s, and Li 1s spectra in **Figure** 12c were a function of potential applied across the cell during discharge from 2.7 (OCV) to 1.0 V_{Li} in CO_2/H_2O gas (5 mbar) and charge from 4.6 to 4.9 V in high-vacuum (HV). They reported that XPS findings for CO_2/H_2O gas were significantly different from those for CO₂ alone. A new peak at ≈284 eV appeared in C 1s region and increased to ≈ 170% at 1.2 V upon discharge. This new peak with sp² hybridization feature is assigned to the amorphous carbon species accompanied with significantly accumulated LiOH species, based on an intensity increase in O 1s region and a gradual shift of Li 1s peak. Similarly, when charging cells in CO_2/O_2 gas, the intensity of amorphous carbon (≈284 eV) gradually increased to ≈ 280% at 1.3 V in C 1s signal. The formation of Li_2O_2 and Li_2O is supported by a gradual shift in Li 1s peak to a lower binding energy, evidencing the change in chemical environment from coordinated by $[TFSI]^-$ to combined by O_2^{2-}/O^{2-}
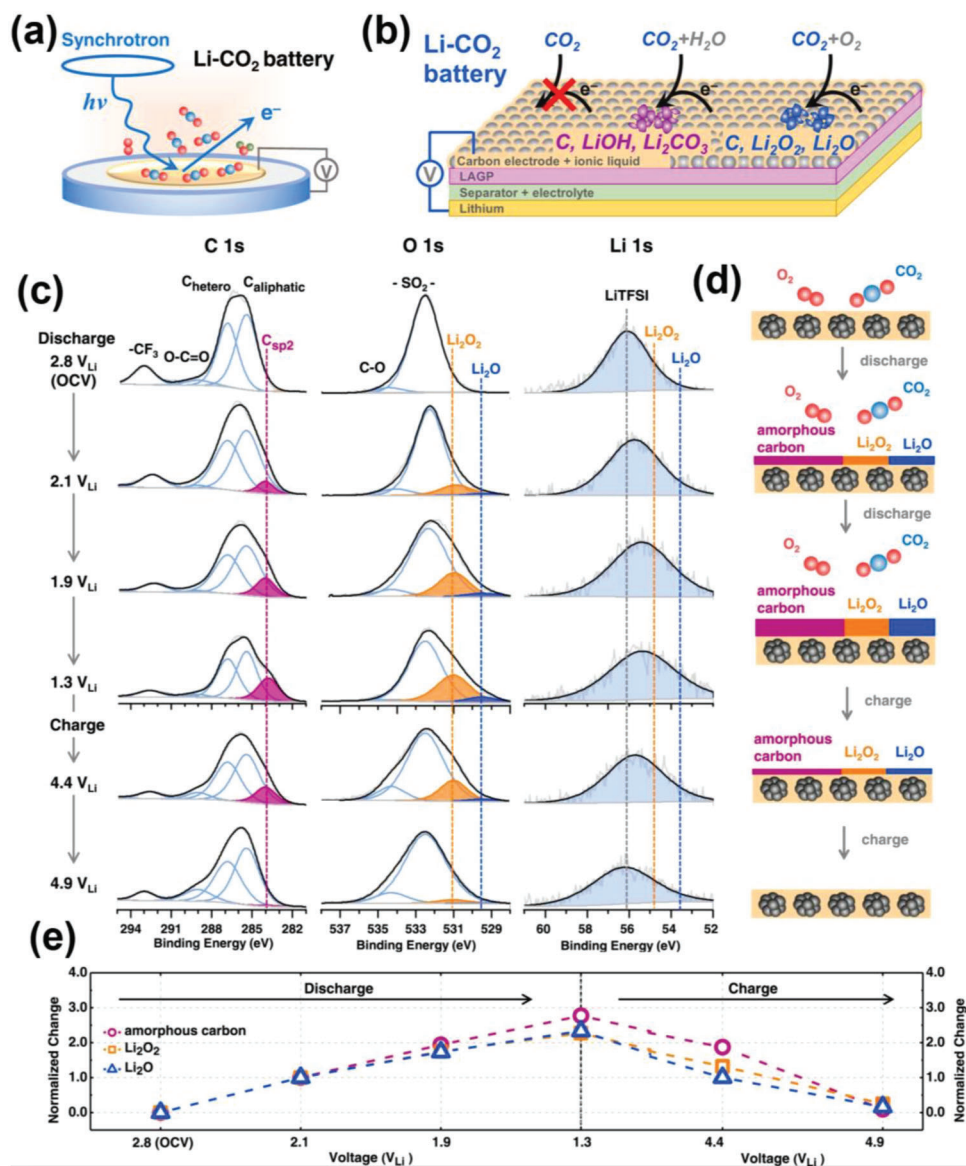
Figure 12. Application of in situ APXPS to quantitatively determine mechanisms for Li–CO$_2$ batteries. a,b) Schematic for in situ APXPS cell. c) In situ APXPS data for C$_{1s}$, O$_{1s}$, and Li$_{1s}$ regions collected on discharging in pressure of p(CO$_2$:O$_2$ = 2:1) = 5 mbar and charging in high vacuum. d) Schematic illustration of the reaction mechanism at different states. e) Normalized intensity changes of C$_{sp2}$, Li$_2$O$_2$, Li$_2$O species in C$_{1s}$ and O$_{1s}$ region. Reproduced with permission.[86] Copyright 2022, Elsevier.

for Li$^+$. Given the fact that it is practically difficult to further reduce Li$_2$O$_2$ to Li$_2$O, the authors proposed a new mechanism that most CO$_2$ was electrochemically reduced to amorphous carbon with the assistance of O$_2$, namely, O$_2$ + CO$_2$ + 6Li$^+$ + 6e$^-$ → C + 2Li$_2$O + Li$_2$O$_2$, with a Gibbs free energy of -1299.2 kJ mol^{-1}. In this case, the charge reaction for amorphous carbon, Li$_2$O$_2$, and Li$_2$O exhibited faster kinetics compared with traditional Li$_2$CO$_3$-oxidation. This work established that APXAS is highly useful for in situ or operando surface study of DPs and intermediates because it provides elemental and chemical composition analysis. However, this sensitive technology has a strong dependency on local reaction conditions, including temperature and pressure gradients, reactant concentration, and mass transport, especially

at the surfaces close to the aperture.[87] Therefore, when applying APXPS for surface characterization in Li–CO$_2$ batteries, a precise control of optimal reaction conditions is necessary to improve sensitivity for in situ and operando study.

The operando XRD serves as a powerful tool to identify and quantify crystalline intermediates and products (such as Li$_2$CO$_3$, Li$_2$O$_2$, Li$_2$O, and Li$_2$C$_2$O$_4$). With high sensitivity and reliability, this technique provides important information about the phase transformation and changes in crystal lattice parameters during cycling. Importantly, both reflection and transmission modes can be used to monitor crystal structure and phase changes of electrodes during battery cycling. In general configurations in operando or operando XRD characterization, Kapton, Mylar, and

**ADVANCED
SCIENCE NEWS**

www.advancedsciencenews.com

**ADVANCED
MATERIALS**

www.advmat.de

aluminum films with stable, low-cost, and nontoxic feature, need to be used to obviate possible sample contamination. However, the contamination of CO_2 containing containers is inevitable in most designs in Li–CO_2 batteries, resulting in practical, analytical problems for operando XRD configurations. This would be the main reason why the application of the operando XRD in Li–CO_2 batteries is rarely reported.

However, it is worth noting that the battery configurations usually determine the battery performance. The in situ batteries, to a certain extent, ensure the in situ detection and analysis at the cost of the battery performance, resulting in larger overpotential and reduced battery capacities. We note that the information about intermediates and by-products by in situ analysis may vary from the real situation and so the revealed mechanism may be misleading. For example, in DEMS analysis, the concentration changes of CO_2 and O_2 are usually small under normal operating conditions (100 or 200 mA g^{-1}). To ensure the detection of gas evolution rates of CO_2 and O_2, the current density is usually set to above 500 mA g^{-1}, resulting in deviated information from that of normal cells. In addition, the APXPS normally operated under relatively low pressure (e.g., 5 mbar), which may limit the concentration of CO_2 in the Li–CO_2 cell. Mass transfer problem of CO_2 during in situ test may result in reduced capacities and enlarged discharge overpotential. Therefore, the operating conditions and battery performances of the in situ cells should be comparable to the normal ones to ensure the representative and typical electrochemical behaviors during in situ measurements. In addition, more evidence from other characterizations operated at normal conditions, such as in situ FTIR and in situ Raman, are encouraged to support findings from techniques operated at special conditions.

5. Control Methods for DP Formation and Decomposition

It is concluded in the foregoing that the electrochemical performance of rechargeable aprotic Li–CO_2 batteries is significantly limited by physicochemical properties of DPs. Adjusting DPs from thermodynamically stable Li_2CO_3 to readily-to-decompose $Li_2C_2O_4$, CO, or formic acid is a practical method to boost battery electrochemical performance. However, the choice of catalyst/electrolyte and reaction conditions is limited. At present, Li_2CO_3 and C remain the most widely observed DPs, although decomposition difficulty restricts improvement of overpotential and the battery stability.

Attempts have been made to control products and facilitate charge /ionic transfer kinetics through the introduction of catalysts, electrolyte engineering, and cell configuration optimization. In this section, prevalent control methods are critically assessed for Li_2CO_3 and C products, together with proposed guidelines for the development of highly reversible and high-efficiency Li–CO_2 batteries.

5.1. Property Modification of Li_2CO_3 & Products

5.1.1. Morphology Control

Ideally, DPs should be readily (and completely) decomposed during charge. To achieve this, the morphology of Li_2CO_3 and C

needs to exhibit properties, namely, 1) particle size "small" (e.g., less than 100 nm); 2) DP layer "thin" (e.g., less than 100 nm) to ensure the contact of catalysts, products, and electrolyte; 3) DPs homogenously distributed on the catalyst surface to obviate shedding from the cathode.

To achieve this, cathode structure needs to be optimized with good conductivity and large surface area with "moderate" porosity and channels to allow rapid diffusion of Li^+ and CO_2 and uniform nucleation/growth of Li_2CO_3 and C. Typically, carbonaceous materials, including pristine CNTs, Ketjen black (KB), carbon nanofibers, super P, and graphene, are favorable because of adjustable electron conductivity, pore structures, and surface activity sites.[88] Chen et al. employed the CO_2-activation method to optimize the structure of nitrogen-doped graphene (NG) material toward high conductivity with large surface area (**Figure 13**a).[37] On conventional NG, Li_2CO_3 nucleates nonuniformly and grows into square nanorod structures with thickness of 200 nm because of poor electrical conductivity and Li^+/CO_2 adsorption. When NG was thermally treated in CO_2, catalysts (CA-NG/RGO) were activated with enlarged surface area and increased electron conductivity with high content of pyridinic-N and pyrrolic-N (72%). The ability of Li^+/CO_2 adsorption based on theoretically computed absorption energy for CO_2, Li, and Li_2CO_3 is also improved (**Figure** 13b). In this way, the uniformly distributed lamellar products with a thickness of 10 nm were formed on the cathode surface. Thus, a low voltage gap of 2.13 V at 1.2 A g^{-1} together with long cycling stability of 170 cycles at 500 mA g^{-1} was achieved as thin nanosheets can be completely decomposed during charge (**Figure** 13c,d). Therefore, cathode structures with excellent conductivity with rich pores and channels are critical for DP morphology optimization.

Favorable geometric features of catalysts in Li–CO_2 batteries play a significant role in DP size control as ultrafine and well-dispersed catalysts are a prerequisite for uniform nucleation and growth of Li_2CO_3 and carbon. Using advanced synthesis technology, ultrafine catalysts with nanoscale, sub-nanoscale, or even single atom scale, can be well dispersed on substrates. To take the maximum advantage of active metal atoms and strong interfacial electronic interactions between catalysts and DPs, Zhou et al. synthesized three types of single-atom catalysts consisting of Fe, Co, and Ni single atoms on reduced graphene oxide (rGO) respectively. Amongst them, the Fe_1/N-RGO with unique metal atom active sites can decrease the Li_2CO_3 size, resulting in a reduced charge overpotential.[69c] Therefore, ultra-fine catalysts with uniform dispersion are important in ensuring uniform nucleation /growth. At present, ultrafine nano /sub-nano catalysts, or single-atom catalysts, are widely used in electrocatalysis, including ORR, OER, HER, and CRR with liquid, or gaseous reactants and products. However, in the Li–CO_2 battery system, a practical problem with ultrafine catalysts is the degradation of active sites caused by coverage of gradually accumulated products. Therefore, it is critical to avoid coverage of active sites and mass transfer problems when optimizing the ultra-fine catalysts.

5.1.2. Electronic Structure Control

The DP decomposition involves bond cleavage of Li–O and C–O in stable triangle structure of Li_2CO_3. To promote the

**ADVANCED
SCIENCE NEWS**

www.advancedsciencenews.com

**ADVANCED
MATERIALS**

www.advmat.de
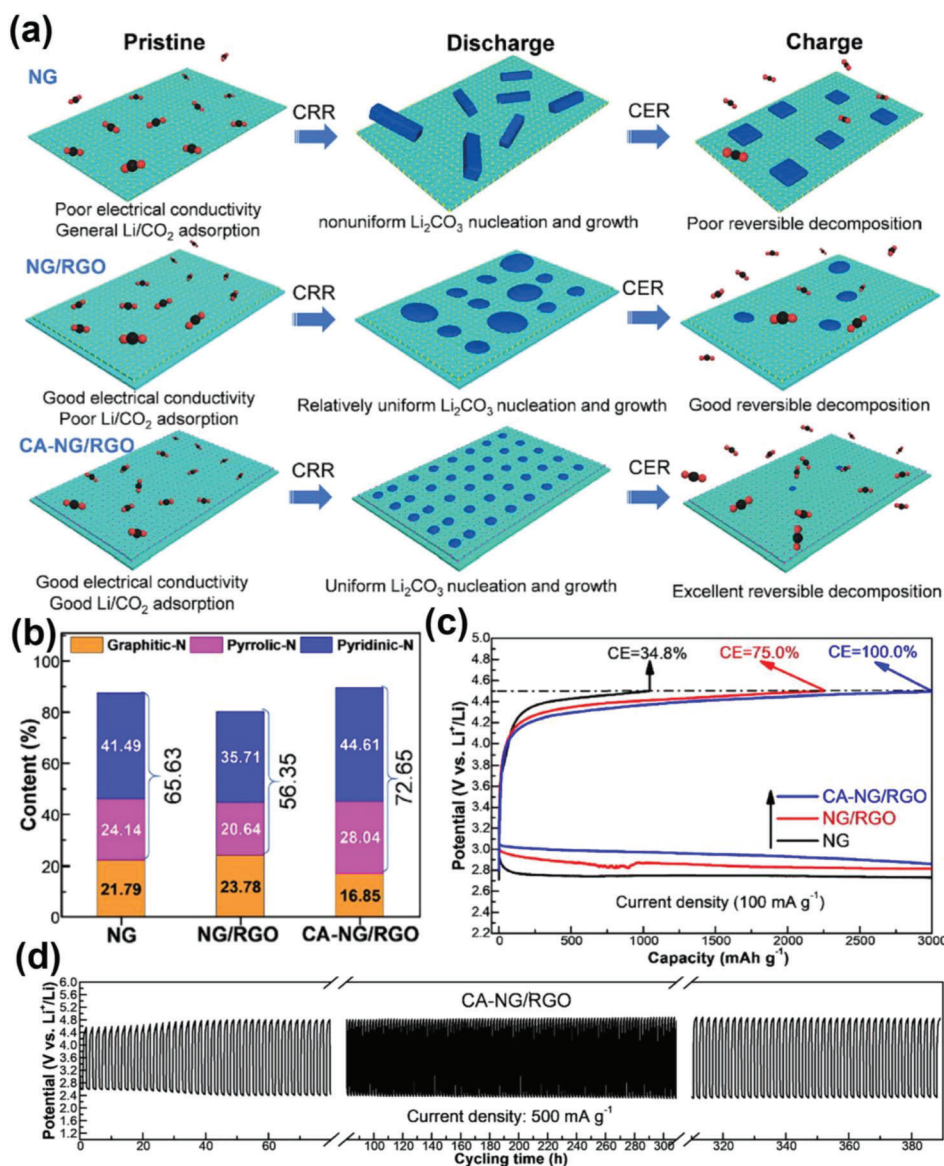
Figure 13. Summary of carbonaceous catalyst for product morphology control in Li–CO_2 batteries. a) DP formation (CRR) and decomposition (CER) on nitrogen-doped graphene (NG), NG and rGO thermal treated in Ar (NG/RGO), and CO_2 activated NG/RGO (CA-NG/RGO) catalysts. b) Atomic contents of pyridinic-N, graphitic-N, and pyrrolic-N of NG, NG/RGO, and CA-NG/RGO catalysts. c) GDC profiles for Li–CO_2 batteries with NG, NG/RGO, and CA-NG/RGO catalyst at 100 mA g^{-1} with a specific capacity limit of 3000 mAh g^{-1}. d) Time-voltage curves at 500 mA g^{-1} for CA-NG/RGO catalysts. Reproduced with permission.[37] Copyright 2021, American Chemical Society.

decomposition, the stable triangle structure of CO_3^{2-} in Li_2CO_3 products needs to be disrupted.

Electron-rich catalysts can help weaken the C–O bonds in the stable triangle. Zhang et al. prepared electron-rich W_2C nanoparticles embedded in walls of carbon nanotubes (**Figure** 14a–e).[20] As is seen in **Figure** 14c,d, XAS and Raman findings demonstrated distinctive W–O bonds are formed, where W atoms come from W_2C (101) surfaces and O atoms come from Li_2CO_3. In this way, the stable triangle structure of CO_3^{2-} is disrupted and the Li_2CO_3 decomposition barrier shown in **Figure** 14b is decreased significantly from ≈3 eV on CNTs to ≈0.7 eV on W_2C/CNTs. As a result, a low charge voltage of 3.2 V and high round trip efficiency

of 90.1% were exhibited (**Figure** 14e). Therefore, the disturbing of C–O in Li_2CO_3 by electron-rich catalysts is effective in promoting the decomposition.

Synergistic effects of nucleophilic and electrophilic species in catalysts can interact with atoms in Li_2CO_3 to boost the bond cleavage during charge. For example, Chen et al. introduced in-plane S vacancy and N dopant centers to NS_V-ReS_2 catalysts to change the stability of CO_3^{2-}.[51] The nucleophilic N dopant center has interaction with Li atoms in intermediates, while the electrophilic S vacancy has interaction with C or O atoms (**Figure** 14f,g). Thus, the dual center of N dopant and S vacancy produces suitable interactions with *$LiCO_2$ and *Li_2CO_2

**ADVANCED
SCIENCE NEWS**

www.advancedsciencenews.com

**ADVANCED
MATERIALS**

www.advmat.de
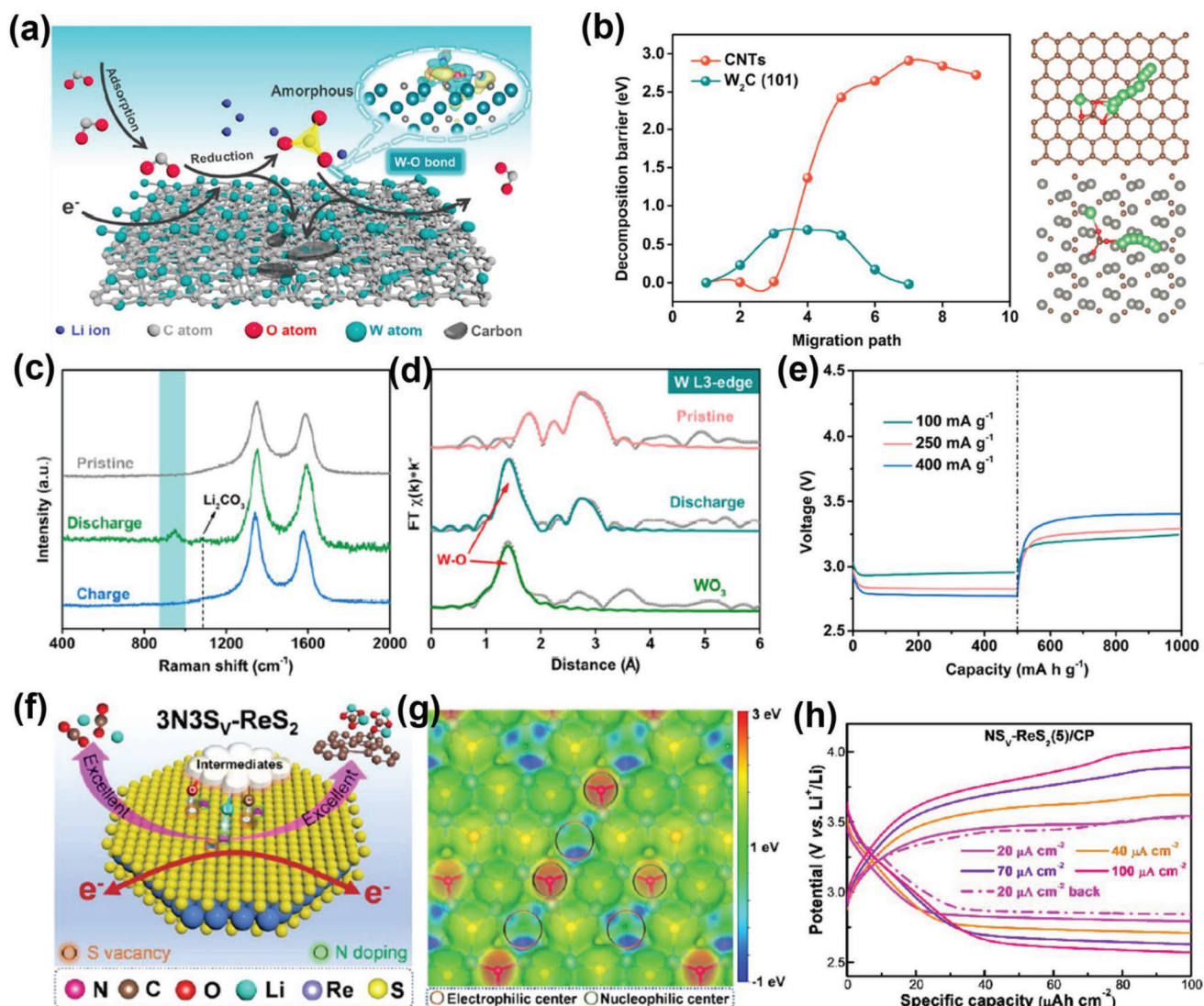
Figure 14. Summary of electron distribution control methods to break stable Li_2CO_3. a) Schematic illustration of W_2C catalysts for amorphous Li_2CO_3 formation and decomposition. b) Decomposition barrier and decomposition on Li_2CO_3 on CNTs and W_2C (101) surfaces, green, brown, red, and gray balls represent Li, C, O, and W atoms, respectively. c) Raman spectra and d) wavelet transform EXAFS of W_2C-CNTs cathodes at different stages. e) GDC profiles under different current densities of W_2C–CNTs cathodes. Reproduced with permission.[20] Copyright 2021, American Chemical Society. f) Illustration of discharge/charge mechanism for nucleophilic N dopant and electrophilic S vacancy dual centers in the $3N3S_V$-ReS_2 plane. g) Surface electrostatic potential diagrams of nucleophilic and electrophilic centers. h) GDC profiles with limited capacity of 100 µAh cm^{-2}. Reproduced with permission.[51] Copyright 2022, American Chemical Society.

intermediates and Li_2CO_3 products, leading to lowered energy barriers for both Li_2CO_3 formation and decomposition. As a result, a small voltage gap of 0.66 V and a high energy efficiency of 81.1% at 20 µA cm^{-2} were exhibited in this system (**Figure** 14h).

In summary, establishing novel catalysts with the interaction between catalysts and Li_2CO_3 is effective for enhancing the CER/CRR electrocatalytic activity in Li–CO_2 batteries. Metal elements with good oxygen affinity (such as Mo, Ti, Sn, Pt) are good candidates for catalyst preparation as strong metal–oxygen bonds can be formed between catalysts and the oxygen in Li_2CO_3.[89] Defect engineerings, such as heterogeneous doping and oxygen vacancies, can also be applied as the active species on the cat-

alyst surface to promote the interaction between catalysts and intermediates.[90]

5.2. Reaction Pathway Modification

5.2.1. Concurrent Decomposition

Decomposition of Li_2CO_3 can be through either solo decomposition or concurrent decomposition with carbon products. The solo decomposition of Li_2CO_3 corresponds to high overpotential (>4 V) and results in the accumulation of amorphous carbon on

**ADVANCED
SCIENCE NEWS**

www.advancedsciencenews.com

**ADVANCED
MATERIALS**

www.advmat.de

the surface of catalysts. However, the concurrent decomposition with the reaction of $4Li^+ + 3CO_2 + 4e^- \leftrightarrow 2Li_2CO_3 + C$ is reversible with lower charge potential. Therefore, it is necessary to develop catalysts that enable a full concurrent decomposition of Li_2CO_3 and C during charge. Ru-based catalysts are reported effective by Qiao et al.[16] In their work, negligible O_2 fragment was detected via GC-MS during charge, evidencing concurrent decomposition of Li_2CO_3 and C. At present, a wide variety of catalysts have been developed by introducing highly active species into catalysts, such as Ni, Co, and Ir to achieve concurrent decomposition.

The contact between catalysts and solid products is another problem that limits the concurrent decomposition and practical interface adjustment needs to be considered to achieve the concurrent decomposition of DPs.[18] Given the solid feature of DPs, introduce of mobile homogenous species to the electrolyte, for example, redox mediators (RMs), is practical to solve the contact problem. During the discharge, the RM is reduced to RM$^-$ before CO_2 reduction. Then the reduced RM$^-$ transfers electrons to Li$^+$ and CO_2 to form RM and DPs. During charge, the RM medium is electrochemically oxidized to RM$^+$. Subsequently, the oxidized RM$^+$ decomposes the Li_2CO_3 and C chemically and releases Li$^+$ ions and CO_2. In this system, the discharge /charge voltage is determined by the redox potential of the RM. Because the RM is homogeneous and flexible, most of DP surfaces can be wrapped in the RM. The poor contact of catalysts and products in the solid catalyst system is obviated in this situation. Wang et al. used LiBr as RM in an electrolyte of 1 M LiTFSI /TEGDME (TEGDME = tetraethylene glycol dimethyl ether).[91] Without LiBr, KB-based cathode in Li–CO_2 batteries was fully covered with the agglomerated DPs, whilst a porous structure was well maintained when the KB cathode operated with LiBr. Additionally, during the redox reaction, Br$^-$ can be continuously oxidized to Br$_3^-$, and finally to Br$_2$. The electrochemically generated Br$_2$ could chemically oxidize the Li_2CO_3 and C by leaving the group of Br$_3^-$ in the electrolyte. With the action of LiBr RMs, the charging potential is significantly decreased by 0.3 V at 100 mA g^{-1} for the first cycle. Lian et al. used ruthenium acetylacetonate (Ru(acac)$_3$) as an innovative RM.[92] The theoretical oxidation potential of Ru(acac)$_3$ is lower than that of TEGDME and LiSO$_3$CF from the calculated highest occupied molecular orbital (HOMO) energy level. The terminal charge voltage of the battery with Ru(acac)$_3$ (3.88 V) is 0.64 V lower than that of the battery without Ru(acac)$_3$. At present, there are several RMs species employed in the electrolyte for Li–CO_2 batteries, such as tris(2,2'-bipyridyl)-dichloro-ruthenium(II) (Ru(bpy)$_3$Cl$_2$), binuclear cobalt phthalocyanine (Bi-CoPc), 2-ethoxyethylamine (EEA), and diphenyl disulfide.[5a,93] Although shuttle effects of RMs can lead to unwanted side reactions at the anode and RMs sometimes can decompose automatically, it does have advantages in solving interface contact problems and reducing reaction overpotential.[94] To exploit the advantages of RM mediators in Li–CO_2 batteries, more stable RM structures and optimization of the membrane for separation are however needed.

The electrolyte used in Li–CO_2 batteries also plays a significant role in promoting concurrent decomposition of DPs. Generally, electrolytes with excellent ionic conductivity and elevated electrochemical stability are favorable. For example, Wang et al. developed a binary molten nitrate electrolyte (LiNO$_3$ /KNO$_3$ mix-

ture) operated at the temperature of 140 °C and studied effects of electrolyte on charging (**Figure 15**).[43] Because of its molten salt feature, this electrolyte provides a high ionic conductivity of 6.29 mS cm^{-1} with elevated electrochemical stability and fast kinetics. In comparison to the sole decomposition mechanism for Li_2CO_3 in organic electrolyte, this molten salt electrolyte achieves concurrent decomposition of Li_2CO_3 and C on super P-based cathode. Thus, the CO_2 evolution reaction potential during charge can be maintained below 3.6 V. However, the disadvantage is the high temperature required in this molten salt system, which limits its further application. Therefore, it is necessary to develop better electrolytes such as ionic liquid or blended electrolytes with different solvents or salts for ambient conditions with the same functions to promote the concurrent decomposition.
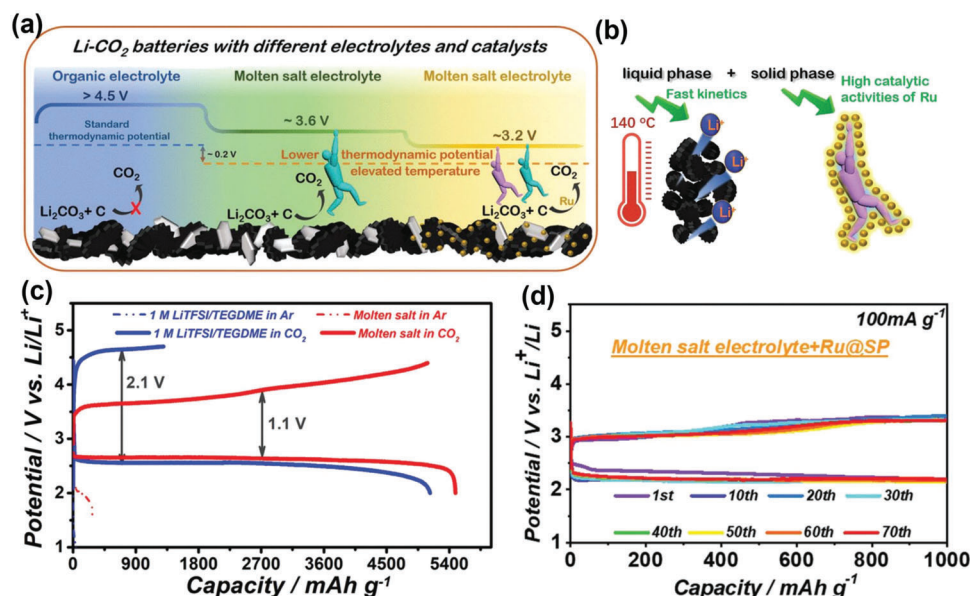
In summary, to promote the concurrent decomposition of DPs, both catalysts and electrolytes should be rationally designed to achieve high activity and address the interface contact problems.

5.2.2. Photoassisted Reaction Pathways

Solar energy can be used to improve the energy conversion and storage in rechargeable batteries as it is inexpensive, environmentally sustainable, and theoretically inexhaustible.[95] Under illumination, photoexcited electrons (e$^-$) and holes (h$^+$) separate into the conduction band (CB) and valance band (VB) of the semiconductor-containing cathode.[96] When solar energy is applied in Li–CO_2 batteries, these active e$^-$ and h$^+$ participate in formation and decomposition of Li_2CO_3, resulting in a significantly decreased reaction barrier.

There are three main solar energy-based strategies that can be used to promote the formation and decomposition of DPs. First of all, semiconductor catalysts with proper band structure can be used to promote the generation of e$^-$ and h$^+$ by photoelectric effects. During the discharge of photoassisted Li–CO_2 batteries, e$^-$ generated at the CB of semiconductor functioning in the CO_2 reduction reaction can optimize the morphology of DPs and boosts the kinetics of subsequent decomposition. The abundant h$^+$ remaining at the VB of the semiconductor participate in decomposition pathways and reduce the charge overpotential.[97] Guan et al. introduced the illumination to a hierarchical porous In$_2$S$_3$@CNT free-standing cathode (ICS) towards flexible Li–CO_2 batteries (**Figure 16**).[98] During discharge, photo excited e$^-$ generates and gathers on the surface of In$_2$S$_3$ to provide increased number of nucleation sites. Then, this e$^-$ combine with the absorbed CO_2 and Li$^+$ to form a thin, film-like Li_2CO_3 and C products with good electronic transmission. During the reverse process, h$^+$ gathered on the electrode surface could promote the decomposition because of the high oxidizing ability. Benefiting from solar energy, the Li–CO_2 battery exhibits an ultrahigh discharge voltage of 3.14 V, and ultralow charge voltage of 3.2 V with the high round-trip efficiency of 98.1%. Therefore, to achieve lower overpotential with excellent stability, exploration of semiconductor catalysts with optimized band structure is practical.

Plasmonic interaction is another photo effect that can be used to assist the decomposition of DPs in Li–CO_2 batteries. Under incident photons at the resonant frequency, localized surface plasmon resonance on Ag and Au nanoparticles, enable

**ADVANCED
SCIENCE NEWS**

www.advancedsciencenews.com

**ADVANCED
MATERIALS**

www.advmat.de

Figure 15. Summary of ultraconductive electrolyte for promotion of concurrent decomposition of Li_2CO_3 and C. a,b) Schematic for comparison of Li–CO_2 batteries in organic and molten salt ($LiNO_3$/KNO_3) electrolyte. c) GDC profiles of the Super P cathode in organic electrolyte and molten salt electrolyte at 100 mA g^{-1}. d) GDC profiles of Ru@Super P cathode in molten salt electrolyte at 100 mA g^{-1}. Reproduced with permission.[43] Copyright 2021, Royal Society of Chemistry.

boosted and tunable electromagnetic fields, light absorption, and scattering.[99] When these localized surface plasmons contact with semiconductors, the separation of e^- and h^+ is promoted, and the recombination via forming a Schottky barrier at the interface is suppressed. As a result, the Li_2CO_3 forma-

tion and decomposition is improved. Moreover, instead of utilizing ultraviolet light (wavelength = 10–400 nm) for semiconductors, this effect enables the application of visible light (wavelength = 400–700 nm) because of the introduction of visible light-sensitive metal particles. Zhang et al. designed a silver
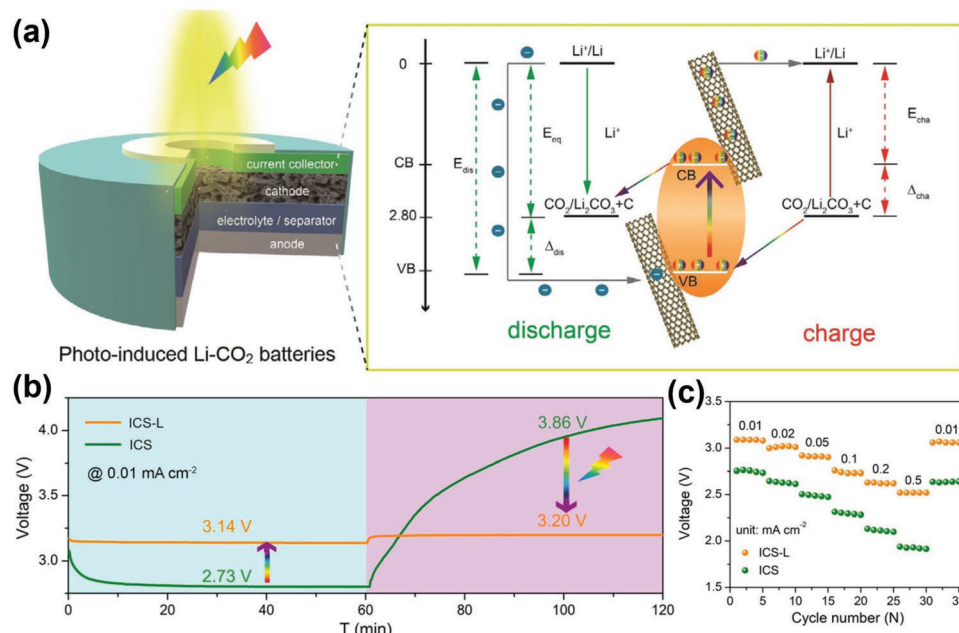
Figure 16. Summary of photoelectric effects on photo-induced Li–CO_2 batteries. a) Schematic illustration of photoinduced Li–CO_2 batteries using In_2S_3@CNT free-standing cathode (ICS) and the energy level diagram for discharge and charge; b) GDC curves for ICS-based Li–CO_2 batteries with/without light at 0.01 mA cm^{-2}. c) Rate performance at different current densities from 0.01 to 0.5 mA cm^{-2}. Reproduced with permission.[98] Copyright 2020, Wiley.

**ADVANCED
SCIENCE NEWS**

www.advancedsciencenews.com

**ADVANCED
MATERIALS**

www.advmat.de
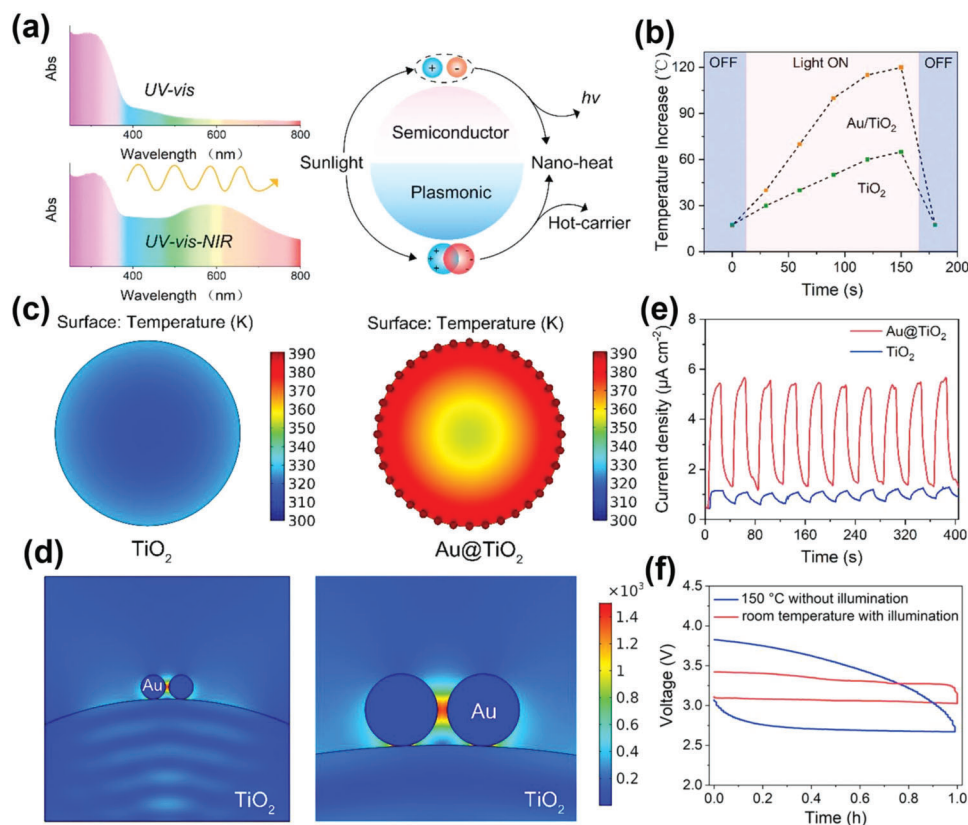
Figure 17. Summary of plasmonic and photothermal effects for Au@TiO$_2$ catalysts in photo-induced Li–CO$_2$ batteries. a) Schematic illustration of the solar-spectrum photothermal effect of Au@TiO$_2$ via plasmon- and exciton-based approaches. b) On /off response of the surface temperature increase of Au@TiO$_2$ and TiO$_2$. c) Distribution of the surface temperature increase on Au@TiO$_2$ and TiO$_2$ under illumination. d) Distribution of the electric near field on Au@TiO$_2$ and TiO$_2$ under illumination. e) Current–time curves on Au@TiO$_2$ and TiO$_2$ and TiO$_2$ surfaces. f) First discharge /charge curves of Li–CO$_2$ batteries working at room temperature with illumination and ≈150 °C without illumination. Reproduced with permission.[100] Copyright 2022, American Chemical Society.

nanoparticle-decorated titanium dioxide nanotube array cathode to realize the synergistic plasmonic interaction and photoelectric effects.[8c] Under incident light, the collective oscillation of free electrons in plasmonic metal nanoparticles could construct a locally intensified electric field to promote the e^- and h^+ separation and transfer, which efficiently participated in the formation and decomposition of Li$_2$CO$_3$ and C through thermodynamically favorable pathways. The resulting Li–CO$_2$ batteries demonstrated ultralow charge voltage of 2.86 V at 0.1 mA m^{-2}. Good cycling stability with round-trip efficiency of 86.9% after 100 cycles was achieved. Therefore, the introduction of plasmonic interaction offers an external driving force to accelerate sluggish cathode kinetics and improve the battery performance.

Photothermal effects are important as well to overcome significant energy barriers and boost CO$_2$ diffusion together with Li$^+$ transfer because battery reactions are temperature sensitive. The photoexcitation of materials results in the conversion of solar energy to thermal energy (heat). When light is applied to Li–CO$_2$ batteries, photothermal effects on DP decomposition cannot be neglected. The photothermal effect significantly overcomes high energy barriers and promotes CO$_2$ diffusion and Li$^+$ transfer. Guan et al. used a photo-assisted all-solid-state Li–CO$_2$ battery by constructing an integrated bilayer Au/TiO$_2$/Li$_{1.5}$Al$_{0.5}$Ge$_{1.5}$(PO$_4$)$_3$

(LAGP)/LAGP (ATLL) framework (**Figure 17**).[100] Except for photoelectric effects in this system, photothermal effects also help accelerate the slow kinetics of Li$_2$CO$_3$-related reactions. Even at an extremely low temperature of -73 °C, the battery can still exhibit a (small) polarization of 0.6 V with a round-trip efficiency of 84.5% by converting solar energy into heat to achieve self-heating. Moreover, because of the synergy of photoelectric and photothermal effects, this all-solid-state Li–CO$_2$ battery can operate within a wide temperature range from -73 to 150 °C utilizing solar energy. The disadvantage is the shorted battery life at high temperature.

In summary, the utilization of light could significantly decrease the charge potential via promoting the DP decomposition. However, in practical charge transfer processes, radiative and nonradiative deactivations on the cathode are inevitable. Direct recombination, indirect recombination, Auger recombination, and surface recombination all decrease the lifetime of separated photoexcited e^- and h^+. Despite progress in spatial separation in photosynthesis and photovoltaics, the rapid recombination remains a practical challenge in photoelectrochemistry.[101] Another limitation is side reactions existed in cathodes, Li anode, and electrolytes. Under illumination, reactive oxygen species, including ^{1}O$_2$ can be generated at the semiconductor surface which induces degradation of electrolyte and catalyst. At the Li anode, Li

**ADVANCED
SCIENCE NEWS**

www.advancedsciencenews.com

**ADVANCED
MATERIALS**

www.advmat.de
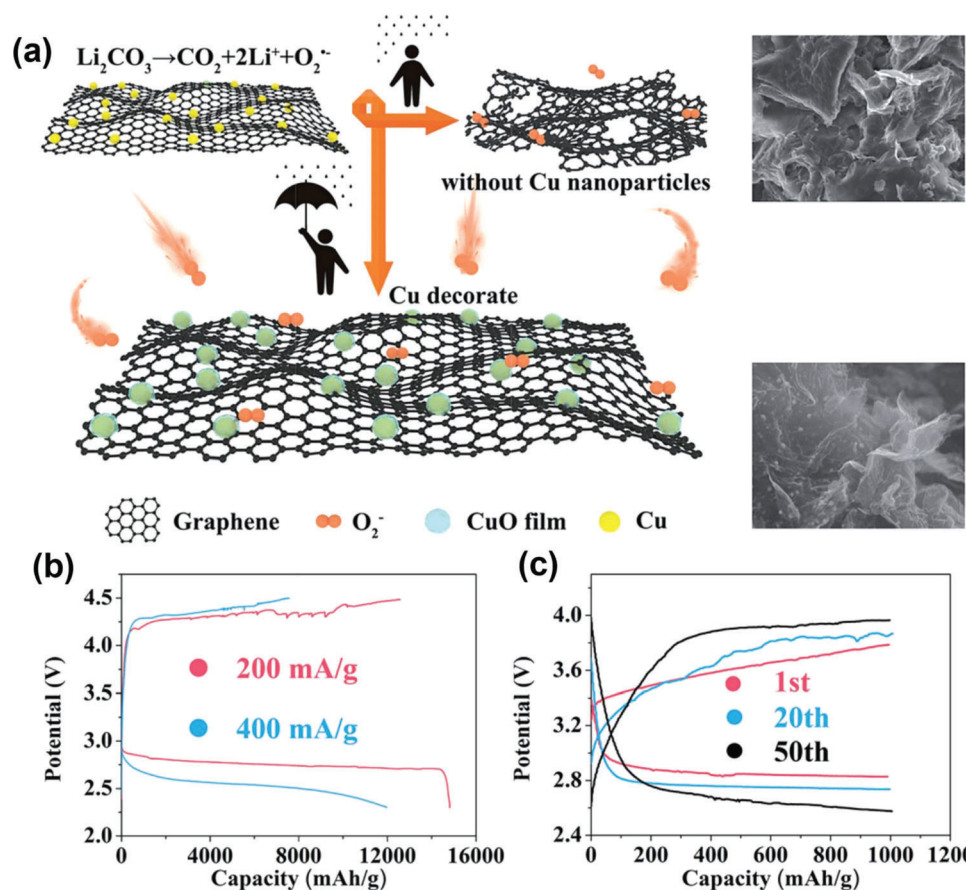
Figure 18. Summary of cathode protection to reduce side reactions and by-products in Li–CO_2 batteries. a) Schematic illustration of Cu-NG as cathode. b) GDC profiles at 200 and 400 mA g^{-1}. c) GDC profiles for Cu-NG cathode with the capacity of 1000 mAh g^{-1} at 200 mA g^{-1}. Reproduced with permission.[102] Copyright 2018, Royal Society of Chemistry.

dendrites can be favored in the presence of active oxygen species, which decreases cycling stability. Therefore, an "ideal" photoassisted Li–CO_2 battery requires stable semiconductor cathode, electrolyte, and Li anode.

5.3. Side Reactions and By-product(s) Control

In aprotic Li–CO_2 batteries, side reactions and related by-products are inevitably generated during discharge and charge. Strong oxidizing species such as $O_2^{\bullet-}$ radicals can attack both electrolytes and cathodes, resulting in numerically more complex side reactions and by-products. Thus, DP decomposition is significantly affected because of the degradation of electrolyte and cathode. The main by-products are oxygen-related radicals that are introduced by O_2 and Li_2CO_3 decomposition (reactions Equations 9, 17, and 18). Thereby, prior to performance testing, battery containers need to be carefully filled with high-purity CO_2 gas, followed by leakage testing, to obviate residual oxygen species in battery containers. Additionally, both Li^+ salts and organic solvents need to be deoxidized and dewatered before battery assembly.

In addition, cathode needs to be protected and stabilized during charge. It is practical to build a thin, porous, and conductive layer on the cathode surface to protect catalysts in Li–CO_2 batteries. Zhang et al. prepared a composite of Cu nanoparticles highly dispersed on N-doped graphene. A CuO film with a thickness of 3–5 nm is formed on Cu nanoparticles to protect Cu catalysts and the N-doped graphene support from the attack of superoxide radicals generated from the self-decomposition of Li_2CO_3, shown in **Figure 18**.[102] As a result, the battery exhibited a low overpotential of 0.77 V, and an excellent 50 cycles (**Figure 18c**). In addition, organic ligands react in a similar way in protecting catalysts from reaction with radicals.[103] Fisher et al. synthesized the copper (II) complex Cu(pyalk)$_2$ (pyalk = 2-pyridyl-2-propanoate) via an oxidation-resistant ligand for water oxidation.[104] The low overpotential of 520–580 mV and excellent stability of 12 h at 1.1 V versus NHE under harsh conditions highlighted the oxidation resistance of the pyalk ligand. The demonstrated effects of pyalk on avoiding reaction with oxidation species are practically promising for development of Li–CO_2 batteries. Importantly, when selecting organic ligands, the mass transportation of CO_2 and Li^+, catalyst activities, and electronic conductivity should not be affected.

Electrolyte stabilizing is another strategy to suppress side reaction or reduce the influence of by-products. Generally, the most used electrolytes for Li–CO_2 batteries are ether-based electrolytes, including TEGDME and DMSO-based electrolytes

because of excellent chemical and thermal stability. Given the high resistance to oxidation, TEGDME exhibits higher oxidation potential (>4.5 V), whilst the DMSO-based electrolyte can readily be oxidized to dimethyl sulfone ($DMSO_2$) by superoxide radical related nucleophilic attack.[16,105] In addition, side reactions between Li anode and DMSO can further deteriorate the battery stability. Therefore, at present TEGDME is the widely used solvent in $Li–CO_2$ batteries. However, the degradation of electrolyte appears likely inevitable, especially at high charge overpotentials. One method to obviate this is to control the interaction between Li salt cations and solvent molecules to protect solvent molecules.[106] For example, Liu et al. assessed lithium salt concentration effects in 1,2-dimethoxyethane (DME)-based electrolytes on cycling stability in $Li–O_2$ batteries.[107] In a highly concentrated electrolyte (LiTFSI concentration: 3 м), all DME molecules were coordinated with salt cations, and the C–H bond scission for DME molecule became increasingly difficult, which protected the electrolyte from the attack of $O_2{}^{.-}$. As a result, the battery cycling stability under both full discharge /charge (2.0–4.5 V vs Li/Li$^+$) and capacity-limited (at 1000 mAh g^{-1}) conditions were significantly enhanced. Moreover, additives that could improve stability during cycling are useful in electrolyte. Wijaya et al. added a gamma fluorinated ether (1,1,1,2,2,3,3,4,4-nonafluoro-6-propoxyhexane) into the TEGDME as electrolyte for $Li–O_2$ batteries.[108] It was identified that this additive helps prevent the attack from superoxide radicals.

In summary, both catalysts and electrolytes are critical in controlling DPs and by-products. New catalysts with specific crystal orientation, optimized coordination environments, and modulated defects, or interfaces will be needed to achieve ultrahigh intrinsic selectivity. Regarding catalyst degradation, a protection layer at the catalyst surface may be effective in practical design. Additionally, to improve the stability of electrolyte, new electrolytes, including ionic liquids, blended electrolytes with optimized ratio, and selected additives need to be employed to improve the cycling performance.

6. Conclusions and Perspectives

Amongst practically promising next-generation batteries, rechargeable lithium–carbon dioxide ($Li–CO_2$) batteries are advantageous because of high-energy storage capability, and CO_2 recyclability. However, electrochemical performance remains limited by large overpotential (>1 V) and poor reversibility during cycling because of decomposition difficulties of thermodynamically stable DPs. This review systematically and comprehensively reviewed discharge /charge mechanisms and demonstrated the impact of DPs in determining the battery performance. Advanced in situ /operando techniques for intermediate and DP identification are essential to illustrate possible mechanisms and rule out false assumptions. We conclude that concurrent decomposition pathways during charge are favorable for battery stability and reversibility, and rational control to tune DPs towards small size, low degree of crystallinity and weakened Li–O and C–O bonds in Li_2CO_3 is needed to boost decomposition and improve performance. In addition, side reactions and by-products should be reduced, and solar energy that can provide extra driving force be used in $Li–CO_2$ batteries.

Based on recent progress in $Li–CO_2$ batteries, perspectives for fundamental study and practical application (**Figure 19**) are presented as follows.

From the viewpoint of fundamentals, the mechanism for nucleation and growth of DPs still lacks direct evidence, which puts forward high requirements for advanced in situ /operando techniques, including in situ SEM, XRD, and XPS. Theoretical computation, for example, DFT computations, will be required to simulate nucleation and growth under complex electrochemical conditions. Additionally, mass transport of Li$^+$ and diffusion of CO_2 in $Li–CO_2$ batteries must be quantitatively better addressed in analyzing formation of DPs. The CO_2 absorption /desorption rate can be described by the mass transfer coefficient.[109] The Li$^+$, CO_2 can be simulated by mesoscopic mass transfer models.[110] To investigate the impacts of CO_2 mass transport, Nernst-Planck equation can be useful to computationally assess the near-surface concentration of molecules during CO_2 reduction.[111]

Decomposition is complex because it involves bond cleavage of Li–O and C–O, and formation of new C–O bonds. Therefore, an improved understanding will be necessary for developing rational design of $Li–CO_2$ batteries. It will be necessary to confirm the rate-determining step for these reactions before designing cathodes for decomposition. Meanwhile, because the decomposition is solid phase reactions occurring at the interface of the cathode, it is necessary to determine the impact(s) of interface contact for performance improvement. Atomic-scale measurements, for example, operando scanning transmission electron microscopy (STEM), will be useful in providing confirmatory evidence on how critical interfaces impact decomposition.[112] If the direct evidence from advanced operando techniques can be judiciously combined with DFT and ab initio-molecular dynamic simulation, more information about the interface for solid phase reaction(s) will be obtained.[113]

Improved understanding of the battery decay mechanism is important to develop stable and practical $Li–CO_2$ batteries. Possible degradation mechanisms can be catalyst agglomeration, active species loss and migration, or contamination of active sites caused by residual DPs. The decomposition of electrolyte at high recharge potential also contributes to unstable performance. Additionally, damage to the separator caused by deposited Li dendrites, electrolyte evaporation, together with blocked channels and pores in gas diffusion layer causes performance decay. It will be important to distinguish which is the overriding factor that determines performance decay by systematic characterizations at different decay status.

For practical application, cathode design is important to product control. To ensure the continuous formation and decomposition of DPs, more stable and active catalysts need to be developed. In recent years, machine learning (ML) has become useful in electrocatalyst screening in areas such as HER, ORR, OER, and CRR.[114] In $Li–CO_2$ batteries, ML techniques will enable computers to learn material electrochemistry and build the relationship between material properties and DP formation /decomposition mechanism without being explicitly programmed. Furthermore, gas diffusion electrodes with enriched pore structures to allow fast CO_2 diffusion and deposition of DPs will need to be reasonably designed.[115] It is practical to build stable three-phase interfaces by reducing diffusion layer thickness to allow fast CO_2
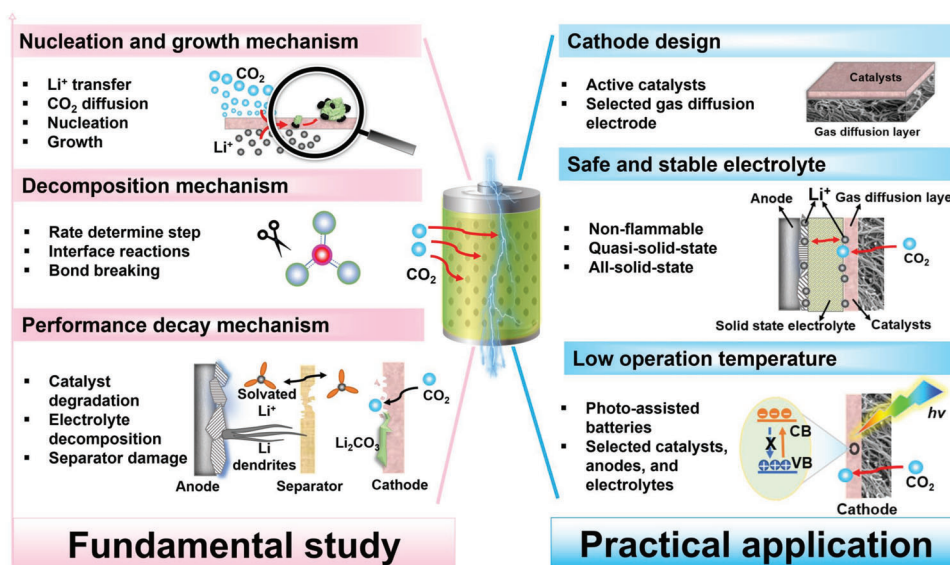
Figure 19. Perspectives of Li–CO$_2$ batteries in the fundamental study and practical applications.

diffusion and Li$^+$ transition without damaging mechanical properties.

Practical electrolyte for Li–CO$_2$ batteries should be safe and stable. Conventional electrolytes consist of highly flammable components that can ignite, leading to serious safety risk. It will be necessary to incorporate flame-retardant additives, including phosphates, fluorides, and fluorinated phosphazenes into the electrolyte, or use nonflammable solvents, such as ionic liquids, to improve safety and stability.[116] In addition, quasi-solid-state batteries with nonflammable gel polymer electrolytes can reduce fire risk and boost the safety and stability. Moreover, all-solid-state batteries using ceramic electrolytes is a practical method for Li–CO$_2$ batteries because of higher thermal stability, electrochemical stability, and high energy density, without leakage risk of electrolyte.

Li–CO$_2$ batteries are practically promising for aerospace exploration on Mars and submarine operation in the deep sea. However, these applications correspond to ultra-low temperature. The main difficulties for low-temperature batteries are slow ion diffusion rate and the consequently sluggish redox kinetics. Therefore, it will be necessary to widen the operation temperature range of Li–CO$_2$ batteries. Suitable Li salt, solvents, and additives which can be adapted to low temperature will need to be developed. Furthermore, it is practical to introduce solar energy as an extra driving force for reactions. Solar energy can be converted to thermal energy to overcome CO$_2$ diffusion and Li$^+$ transfer problem at low temperatures. Suitable catalysts will need to be selected, however, to make use of theoretically inexhaustible solar energy.

To sum up, DPs are closely correlated with the electrochemical performance of Li–CO$_2$ batteries, and therefore the control of DPs is critical for performance improvement. At present, product control strategies are not widely reported because of the limited knowledge of formation/decomposition mechanism(s). However, with the guidance of theoretical study and the identification of in situ /operando techniques, we believe more efficient and practical Li–CO$_2$ systems will be developed and become one of the mainstreams in the next-generation electrochemical energy storage.

Conflict of Interest

The authors declare no conflict of interest.

Keywords

[1] a) W. A. Smith, T. Burdyny, D. A. Vermaas, H. Geerlings, *Joule* **2019**, *3*, 1822; b) L. Jeffry, M. Y. Ong, S. Nomanbhay, M. Mofijur, M. Mubashir, P. L. Show, *Fuel* **2021**, *301*, 121017.

[2] a) J. Lv, J. Xie, A. G. A. Mohamed, X. Zhang, Y. Wang, *Chem. Soc. Rev.* **2022**, *51*, 1511; b) F. A. Canales, J. K. Jurasz, M. Guezgouz, A. Beluco, *Sustainable Energy Technol.* **2021**, *44*, 101062.

[3] a) G. Liang, E. Olsson, J. Zou, Z. Wu, J. Li, C.-Z. Lu, A. M. D'Angelo, B. Johannessen, L. Thomsen, B. Cowie, *Angew. Chem., Int. Ed.* **2022**,

2210671 (30 of 33)

61, e202201969; b) D. Yuan, Y. Dou, Z. Wu, Y. Tian, K.-H. Ye, Z. Lin, S. X. Dou, S. Zhang, *Chem. Rev.* **2021**, *122*, 957; c) G. Liang, V. K. Peterson, Z. Wu, S. Zhang, J. Hao, C. Z. Lu, C. H. Chuang, J. F. Lee, J. Liu, G. Leniec, *Adv. Mater.* **2021**, *33*, 2101413.

[4] a) C. J. Fetrow, C. Carugati, X.-D. Zhou, S. Wei, *Energy Storage Mater.* **2021**, *45*, 911; b) F. Wang, Y. Li, X. Xia, W. Cai, Q. Chen, M. Chen, *Adv. Energy Mater.* **2021**, *11*, 2100667; c) J. Xie, Z. Zhou, Y. Wang, *Adv. Funct. Mater.* **2020**, *30*, 1908285.

[5] a) D. Zhang, W. L. Bai, Z. P. Cai, J. H. Cheng, H. Y. Kuang, B. X. Dong, Y. B. Wang, K. X. Wang, J. S. Chen, *Angew. Chem., Int. Ed.* **2021**, *60*, 16404; b) X. Sun, P. Hou, P. He, H. Zhou, *Energy Fuel* **2021**, *35*, 9165.

[6] K. Takechi, T. Shiga, T. Asaoka, *Chem. Commun.* **2011**, *47*, 3463.

[7] S. Xu, S. K. Das, L. A. Archer, *RSC Adv.* **2013**, *3*, 6656.

[8] a) Q. Q. Hao, Z. Zhang, Y. Mao, K. X. Wang, *ChemNanoMat* **2022**, *8*, 202100381; b) D. Mao, Z. He, W. Lu, Q. Zhu, *Nanomaterials* **2022**, *12*, 2063; c) K. Zhang, J. Li, W. Zhai, C. Li, Z. Zhu, X. Kang, M. Liao, L. Ye, T. Kong, C. Wang, *Angew. Chem., Int. Ed.* **2022**, *61*, e202201718; d) W. Zhang, F. Zhang, S. Liu, W. K. Pang, Z. Lin, Z. Guo, L. Chai, *Proc. Natl. Acad. Sci. USA* **2023**, *120*, e2219692120.

[9] a) F. Cai, Z. Hu, S. L. Chou, *Adv. Sustainable Syst.* **2018**, *2*, 1800060; b) X. Mu, H. Pan, P. He, H. Zhou, *Adv. Mater.* **2020**, *32*, 1903790.

[10] a) Z. Lian, Y. Pei, S. Ma, Y. Lu, Q. Liu, *ChemistrySelect* **2022**, *7*, 202104549; b) Q. Deng, Y. Yang, C. Mao, T. Wang, Z. Fang, W. Yan, K. Yin, Y. Zhang, *Adv. Energy Mater.* **2022**, *12*, 2103667.

[11] J. Wang, Y. Zhai, F. Dang, L. Zhao, Q. Xia, D. Li, D. Zhuang, X. Zhang, *Mater. Lab* **2022**, *1*, 220010.

[12] J. Cheng, Y. Bai, Y. Lian, Y. Ma, Z. Yin, L. Wei, H. Sun, Y. Su, Y. Gu, P. Kuang, *ACS Appl. Mater. Interfaces* **2022**, *14*, 18561.

[13] a) Y. Hou, J. Wang, L. Liu, Y. Liu, S. Chou, D. Shi, H. Liu, Y. Wu, W. Zhang, J. Chen, *Adv. Funct. Mater.* **2017**, *27*, 1700564; b) C. Yang, K. Guo, D. Yuan, J. Cheng, B. Wang, *J. Am. Chem. Soc.* **2020**, *142*, 6983; c) H. Xue, H. Gong, X. Lu, B. Gao, T. Wang, J. He, Y. Yamauchi, T. Sasaki, R. Ma, *Adv. Energy Mater.* **2021**, *11*, 2101630; d) J. Zhou, X. Li, C. Yang, Y. Li, K. Guo, J. Cheng, D. Yuan, C. Song, J. Lu, B. Wang, *Adv. Mater.* **2019**, *31*, 1804439.

[14] a) W.-H. Wang, Y. Himeda, J. T. Muckerman, G. F. Manbeck, E. Fujita, *Chem. Rev.* **2015**, *115*, 12936; b) L. C. Pardo Pérez, A. Teschner, E. Willinger, A. Guiet, M. Driess, P. Strasser, A. Fischer, *Adv. Funct. Mater.* **2021**, *31*, 2103601; c) J. Bok, S. Y. Lee, B.-H. Lee, C. Kim, D. L. T. Nguyen, J. W. Kim, E. Jung, C. W. Lee, Y. Jung, H. S. Lee, *J. Am. Chem. Soc.* **2021**, *143*, 5386.

[15] a) S. Zhang, L. Sun, Q. Fan, F. Zhang, Z. Wang, J. Zou, S. Zhao, J. Mao, Z. Guo, *Nano Res. Energy* **2022**, *1*, e912001; b) Y. Jiao, J. Qin, H. M. K. Sari, D. Li, X. Li, X. Sun, *Energy Storage Mater.* **2021**, *34*, 148.

[16] Y. Qiao, J. Yi, S. Wu, Y. Liu, S. Yang, P. He, H. Zhou, *Joule* **2017**, *1*, 359.

[17] a) A. Hu, W. Lv, T. Lei, W. Chen, Y. Hu, C. Shu, X. Wang, L. Xue, J. Huang, X. Du, *ACS Nano* **2020**, *14*, 3490; b) Y. Dou, X.-G. Wang, D. Wang, Q. Zhang, C. Wang, G. Chen, Y. Wei, Z. Zhou, *Chem. Eng. Sci.* **2021**, *409*, 128145.

[18] S. Ma, Y. Lu, H. Yao, Y. Si, Q. Liu, Z. Li, *J. Energy Chem.* **2021**, *65*, 472.

[19] a) Z. Lian, Y. Lu, C. Wang, X. Zhu, S. Ma, Z. Li, Q. Liu, S. Zang, *Adv. Sci.* **2021**, *8*, 2102550; b) C. Wang, Y. Shang, Y. Lu, L. Qu, H. Yao, Z. Li, Q. Liu, *J. Power Sources* **2020**, *475*, 228703.

[20] X. Zhang, T. Wang, Y. Yang, X. Zhang, Z. Lu, J. Wang, C. Sun, Y. Diao, X. Wang, J. Yao, *ACS Energy Lett.* **2021**, *6*, 3503.

[21] X. Xiao, P. Tan, X. Zhu, Y. Dai, C. Cheng, M. Ni, *ACS Sustainable Chem. Eng.* **2020**, *8*, 9742.

[22] M. Wu, J. Y. Kim, H. Park, D. Y. Kim, K. M. Cho, E. Lim, O. B. Chae, S. Choi, Y. Kang, J. Kim, *ACS Appl. Mater. Interfaces* **2020**, *12*, 32633.

[23] G. Qi, J. Zhang, L. Chen, B. Wang, J. Cheng, *Adv. Funct. Mater.* **2022**, *32*, 2112501.

[24] a) L.-Z. Chen, X.-X. Cao, Y.-Y. Dan, *J. Chem. Res.* **2015**, *39*, 14; b) M. Goodarzi, F. Nazari, F. Illas, *J. Phys. Chem. C* **2018**, *122*, 25776; c) R. Angamuthu, P. Byers, M. Lutz, A. L. Spek, E. Bouwman, *Science* **2010**, *327*, 313.

[25] J. Xie, Q. Liu, Y. Huang, M. Wu, Y. Wang, *J. Mater. Chem. A* **2018**, *6*, 13952.

[26] Z. Zhao, L. Pang, Y. Su, T. Liu, G. Wang, C. Liu, J. Wang, Z. Peng, *ACS Energy Lett.* **2022**, *7*, 624.

[27] a) D. Liuzzi, E. Fernandez, S. Perez, E. Ipiñazar, A. Arteche, J. L. G. Fierro, J. L. Viviente, D. A. P. Tanaka, S. Rojas, *Rev. Chem. Eng.* **2022**, *38*, 55; b) J. Wentrup, G. R. Pesch, J. Thöming, *Renewable Sustainable Energy Rev.* **2022**, *162*, 112454; c) B. Liu, Y. Zhang, J. Wang, J. Wang, Z. Su, G. Li, T. Jiang, *Appl. Surf. Sci.* **2018**, *444*, 133; d) M. C. Monteiro, M. F. Philips, K. J. P. Schouten, M. Koper, *Nat. Commun.* **2021**, *12*, 4943; e) G. Marcandalli, A. Goyal, M. T. Koper, *ACS Catal.* **2021**, *11*, 4936; f) Y. Chen, J. Wei, M. S. Duyar, V. V. Ordomsky, A. Y. Khodakov, J. Liu, *Chem. Soc. Rev.* **2021**, *50*, 2337.

[28] a) S. Nitopi, E. Bertheussen, S. B. Scott, X. Liu, A. K. Engstfeld, S. Horch, B. Seger, I. E. Stephens, K. Chan, C. Hahn, *Chem. Rev.* **2019**, *119*, 7610; b) W. Ren, C. Zhao, *Natl. Sci. Rev.* **2020**, *7*, 7.

[29] a) N. Han, P. Ding, L. He, Y. Li, Y. Li, *Adv. Energy Mater.* **2020**, *10*, 1902338; b) L. Li, A. Ozden, S. Guo, F. P. Garciá de Arquer, C. Wang, M. Zhang, J. Zhang, H. Jiang, W. Wang, H. Dong, D. Sinton, E. H. Sargent, M. Zhong, *Nat. Commun.* **2021**, *12*, 5223; c) W. Ma, S. Xie, X.-G. Zhang, F. Sun, J. Kang, Z. Jiang, Q. Zhang, D.-Y. Wu, Y. Wang, *Nat. Commun.* **2019**, *10*, 892; d) K. Fan, Y. Jia, Y. Ji, P. Kuang, B. Zhu, X. Liu, J. Yu, *ACS Catal.* **2019**, *10*, 358.

[30] a) N. Han, P. Ding, L. He, Y. Li, Y. Li, *Adv. Energy Mater.* **2020**, *10*, 1902338; b) Y. Zhou, R. Zhou, X. Zhu, N. Han, B. Song, T. Liu, G. Hu, Y. Li, J. Lu, Y. Li, *Adv. Mater.* **2020**, *32*, 2000992.

[31] a) J. Zou, C. Y. Lee, G. G. Wallace, *Adv. Sci.* **2021**, *8*, 2004521; b) Y. Wang, L. Xu, L. Zhan, P. Yang, S. Tang, M. Liu, X. Zhao, Y. Xiong, Z. Chen, Y. Lei, *Nano Energy* **2022**, *92*, 106780.

[32] F. Zhang, A. C. Co, *Angew. Chem., Int. Ed.* **2020**, *59*, 1674.

[33] a) M. Ramdin, A. R. Morrison, M. De Groen, R. Van Haperen, R. De Kler, E. Irtem, A. T. Laitinen, L. J. Van Den Broeke, T. Breugelmans, J. M. Trusler, *Ind. Eng. Chem. Res.* **2019**, *58*, 22718; b) Y. J. Sa, C. W. Lee, S. Y. Lee, J. Na, U. Lee, Y. J. Hwang, *Chem. Soc. Rev.* **2020**, *49*, 6632; c) D. Gao, R. M. Arán-Ais, H. S. Jeon, B. Roldan Cuenya, *Nat. Catal.* **2019**, *2*, 198.

[34] C.-T. Dinh, T. Burdyny, M. G. Kibria, A. Seifitokaldani, C. M. Gabardo, F. P. García de Arquer, A. Kiani, J. P. Edwards, P. De Luna, O. S. Bushuyev, *Science* **2018**, *360*, 783.

[35] a) J. Zhang, W. Luo, A. Züttel, *J. Catal.* **2020**, *385*, 140; b) D. M. Weekes, D. A. Salvatore, A. Reyes, A. Huang, C. P. Berlinguette, *Acc. Chem. Res.* **2018**, *51*, 910.

[36] X. Xiao, Z. Zhang, P. Tan, *Proc. Natl. Acad. Sci. USA* **2023**, *120*, e2217454120.

[37] B. Chen, D. Wang, B. Zhang, X. Zhong, Y. Liu, J. Sheng, Q. Zhang, X. Zou, G. Zhou, H.-M. Cheng, *ACS Nano* **2021**, *15*, 9841.

[38] J. Zhang, F. Wang, G. Qi, J. Cheng, L. Chen, H. Liu, B. Wang, *Adv. Funct. Mater.* **2021**, *31*, 2101423.

[39] F. Ye, L. Gong, Y. Long, S. N. Talapaneni, L. Zhang, Y. Xiao, D. Liu, C. Hu, L. Dai, *Adv. Energy Mater.* **2021**, *11*, 2101390.

[40] Z. Hu, Y. Xie, D. Yu, Q. Liu, L. Zhou, K. Zhang, P. Li, F. Hu, L. Li, S. Chou, *ACS Nano* **2021**, *15*, 8407.

[41] C. Chen, J. F. K. Kotyk, S. W. Sheehan, *Chem* **2018**, *4*, 2571.

[42] X. Li, J. Zhang, G. Qi, J. Cheng, B. Wang, *Energy Storage Mater.* **2021**, *35*, 148.

[43] D. Wang, J. Yang, P. He, H. Zhou, *Energy Environ. Sci.* **2021**, *14*, 4107.

[44] J. Lin, J. Ding, H. Wang, X. Yang, X. Zheng, Z. Huang, W. Song, J. Ding, X. Han, W. Hu, *Adv. Mater.* **2022**, *34*, 2200559.

[45] Y. Zhai, H. Tong, J. Deng, G. Li, Y. Hou, R. Zhang, J. Wang, Y. Lu, K. Liang, P. Chen, *Energy Storage Mater.* **2021**, *43*, 391.

[46] C. Wang, Q. Zhang, X. Zhang, X. G. Wang, Z. Xie, Z. Zhou, *Small* **2018**, *14*, 1800641.

[47] Y. Mao, C. Tang, Z. Tang, J. Xie, Z. Chen, J. Tu, G. Cao, X. Zhao, *Energy Storage Mater.* **2019**, *18*, 405.

[48] B. W. Zhang, Y. Jiao, D. L. Chao, C. Ye, Y. X. Wang, K. Davey, H. K. Liu, S. X. Dou, S. Z. Qiao, *Adv. Funct. Mater.* **2019**, *29*, 1904206.

[49] L. Liu, L. Zhang, K. Wang, H. Wu, H. Mao, L. Li, Z. Sun, S. Lu, D. Zhang, W. Yu, *ACS Appl. Mater. Interfaces* **2020**, *12*, 33846.

[50] Z. Zhang, X. G. Wang, X. Zhang, Z. Xie, Y. N. Chen, L. Ma, Z. Peng, Z. Zhou, *Adv. Sci.* **2018**, *5*, 1700567.

[51] B. Chen, D. Wang, J. Tan, Y. Liu, M. Jiao, B. Liu, N. Zhao, X. Zou, G. Zhou, H.-M. Cheng, *J. Am. Chem. Soc.* **2022**, *144*, 3106.

[52] Y. Liu, S. Zhao, D. Wang, B. Chen, Z. Zhang, J. Sheng, X. Zhong, X. Zou, S. P. Jiang, G. Zhou, *ACS Nano* **2021**, *16*, 1523.

[53] Z. Zhao, Y. Su, Z. Peng, *J. Phys. Chem. Lett.* **2019**, *10*, 322.

[54] Y. Qiao, S. Xu, Y. Liu, J. Dai, H. Xie, Y. Yao, X. Mu, C. Chen, D. J. Kline, E. M. Hitz, *Energy Environ. Sci.* **2019**, *12*, 1100.

[55] K. Takechi, S. Higashi, F. Mizuno, H. Nishikoori, H. Iba, T. Shiga, *ECS Electrochem. Lett.* **2012**, *1*, A27.

[56] N. Feng, P. He, H. Zhou, *Adv. Energy Mater.* **2016**, *6*, 1502303.

[57] H.-K. Lim, H.-D. Lim, K.-Y. Park, D.-H. Seo, H. Gwon, J. Hong, W. A. Goddard III, H. Kim, K. Kang, *J. Am. Chem. Soc.* **2013**, *135*, 9733.

[58] S. Ma, H. Yao, D. Lei, X. Guo, Y. Lu, Q. Liu, Z. Li, *Chem. Commun.* **2018**, *54*, 8072.

[59] H. Wang, K. Xie, Y. You, Q. Hou, K. Zhang, N. Li, W. Yu, K. P. Loh, C. Shen, B. Wei, *Adv. Energy Mater.* **2019**, *9*, 1901806.

[60] S. Meini, N. Tsiouvaras, K. U. Schwenke, M. Piana, H. Beyer, L. Lange, H. A. Gasteiger, *Phys. Chem. Chem. Phys.* **2013**, *15*, 11478.

[61] M. Kim, E. Yoo, W.-S. Ahn, S. E. Shim, *J. Power Sources* **2018**, *389*, 20.

[62] X. Xiao, W. Yu, W. Shang, P. Tan, Y. Dai, C. Cheng, M. Ni, *Energy Fuels* **2020**, *34*, 16870.

[63] a) J. Li, Z. Kong, X. Liu, B. Zheng, Q. H. Fan, E. Garratt, T. Schuelke, K. Wang, H. Xu, H. Jin, *InfoMat* **2021**, *3*, 1333; b) S. Qian, C. Xing, M. Zheng, Z. Su, H. Chen, Z. Wu, C. Lai, S. Zhang, *Adv. Energy Mater.* **2022**, *12*, 2103480; c) H. Wan, Y. Sun, W. Cai, Q. Shi, Y. Zhu, Y. Qian, *Adv. Funct. Mater.* **2022**, *32*, 2106984.

[64] R. Chen, Q. Li, X. Yu, L. Chen, H. Li, *Chem. Rev.* **2019**, *120*, 6820.

[65] a) R. Black, S. H. Oh, J.-H. Lee, T. Yim, B. Adams, L. F. Nazar, *J. Am. Chem. Soc.* **2012**, *134*, 2902; b) Y. Chen, S. A. Freunberger, Z. Peng, F. Bardé, P. G. Bruce, *J. Am. Chem. Soc.* **2012**, *134*, 7952.

[66] a) M. Ue, H. Asahina, S. Matsuda, K. Uosaki, *RSC Adv.* **2020**, *10*, 42971; b) N. Mozhzhukhina, L. P. Méndez De Leo, E. J. Calvo, *J. Phys. Chem. C* **2013**, *117*, 18375.

[67] Z. Wang, S. Tian, B. Shao, S. Li, L. Li, J. Yang, *J. Power Sources* **2019**, *414*, 327.

[68] a) P. Zhang, B. Han, X. Yang, Y. Zou, X. Lu, X. Liu, Y. Zhu, D. Wu, S. Shen, L. Li, *J. Am. Chem. Soc.* **2022**, *144*, 2129; b) Y. S. Hong, C. Z. Zhao, Y. Xiao, R. Xu, J. J. Xu, J. Q. Huang, Q. Zhang, X. Yu, H. Li, *Batteries Supercaps* **2019**, *2*, 638.

[69] a) S. Basak, J. Jansen, Y. Kabiri, H. W. Zandbergen, *Ultramicroscopy* **2018**, *188*, 52; b) B. Ge, Y. Sun, J. Guo, X. Yan, C. Fernandez, Q. Peng, *Small* **2019**, *15*, 1902220; c) L. Zhou, H. Wang, K. Zhang, Y. Qi, C. Shen, T. Jin, K. Xie, *Sci. China Mater.* **2021**, *64*, 2139.

[70] a) R. Pipes, J. He, A. Bhargav, A. Manthiram, *ACS Appl. Energy Mater.* **2019**, *2*, 8685; b) Y. Zhang, R.-L. Zhong, M. Lu, J.-H. Wang, C. Jiang, G.-K. Gao, L.-Z. Dong, Y. Chen, S.-L. Li, Y.-Q. Lan, *ACS Cent. Sci.* **2020**, *7*, 175; c) Z. Zhuo, K. Dai, R. Qiao, R. Wang, J. Wu, Y. Liu, J. Peng, L. Chen, F. Pan, Z.-x. Shen, *Joule* **2021**, *5*, 975; d) G. Liang, J. Hao, A. M. D'Angelo, V. K. Peterson, Z. Guo, W. K. Pang, *Batteries Supercaps* **2021**, *4*, 380; e) H. Yang, Z. Chen, P. Guo, B. Fei, R. Wu, *Appl. Catal., B* **2020**, *261*, 118240.

[71] a) S. Liu, J. Mao, Q. Zhang, Z. Wang, W. K. Pang, L. Zhang, A. Du, V. Sencadas, W. Zhang, Z. Guo, *Angew. Chem., Int. Ed.* **2020**, *59*, 3638;

b) S. Liu, R. Zhang, J. Mao, Y. Zhao, Q. Cai, Z. Guo, *Sci. Adv.* **2022**, *8*, eabn5097; c) S. Liu, J. Mao, W. K. Pang, J. Vongsvivut, X. Zeng, L. Thomsen, Y. Wang, J. Liu, D. Li, Z. Guo, *Adv. Funct. Mater.* **2021**, *31*, 2104281; d) Z. Wu, G. Liang, W. K. Pang, T. Zhou, Z. Cheng, W. Zhang, Y. Liu, B. Johannessen, Z. Guo, *Adv. Mater.* **2020**, *32*, 1905632.

[72] Y. Qiao, Y. Liu, C. Chen, H. Xie, Y. Yao, S. He, W. Ping, B. Liu, L. Hu, *Adv. Funct. Mater.* **2018**, *28*, 1805899.

[73] a) Y. Qiao, J. Wu, J. Zhao, Q. Li, P. Zhang, C. Hao, X. Liu, S. Yang, Y. Liu, *Energy Storage Mater.* **2020**, *27*, 133; b) Z. Zhang, Q. Zhang, Y. Chen, J. Bao, X. Zhou, Z. Xie, J. Wei, Z. Zhou, *Angew. Chem., Int. Ed.* **2015**, *127*, 6650.

[74] a) R. R. Jones, D. C. Hooper, L. Zhang, D. Wolverson, V. K. Valev, *Nanoscale Res. Lett.* **2019**, *14*, 231; b) D. Cialla-May, M. Schmitt, J. Popp, *Phys. Sci. Rev.* **2019**, *4*, 20170040.

[75] a) D. Kurouski, A. Dazzi, R. Zenobi, A. Centrone, *Chem. Soc. Rev.* **2020**, *49*, 3315; b) M. J. Baker, H. J. Byrne, J. Chalmers, P. Gardner, R. Goodacre, A. Henderson, S. G. Kazarian, F. L. Martin, J. Moger, N. Stone, *Analyst* **2018**, *143*, 1735.

[76] a) S. Anantharaj, K. Karthick, M. Venkatesh, T. V. Simha, A. S. Salunke, L. Ma, H. Liang, S. Kundu, *Nano Energy* **2017**, *39*, 30; b) J. Wang, L. Ma, J. Xu, Y. Xu, K. Sun, Z. Peng, *SusMat* **2021**, *1*, 345; c) Z. Zhao, X. Zhang, Z. Zhou, E. Wang, Z. Peng, *Nano Lett.* **2021**, *22*, 501.

[77] Y. Wang, J. Zhou, C. Lin, B. Chen, Z. Guan, A. M. Ebrahim, G. Qian, C. Ye, L. Chen, Y. Ge, Q. Yun, X. Wang, X. Zhou, G. Wang, K. Li, P. Lu, Y. Ma, Y. Xiong, T. Wang, L. Zheng, S. Chu, Y. Chen, B. Wang, C.-S. Lee, Y. Liu, Q. Zhang, Z. Fan, *Adv. Funct. Mater.* **2022**, *32*, 2202737.

[78] J. Yu, C. Liu, X. Hu, T. Yuan, Y. Zhang, Z. Wang, W. Ji, *Int. J. Electrochem. Sci.* **2021**, *16*, 2.

[79] a) D. G. Kwabi, V. S. Bryantsev, T. P. Batcho, D. M. Itkis, C. V. Thompson, Y. Shao-Horn, *Angew. Chem., Int. Ed.* **2016**, *128*, 3181; b) S. Sankarasubramanian, J. Seo, F. Mizuno, N. Singh, J. Prakash, *J. Phys. Chem. C* **2017**, *121*, 4789.

[80] a) M. C. Sung, G. H. Lee, D. W. Kim, *InfoMat* **2021**, *3*, 1295; b) Y. Lin, Q. Yang, F. Geng, H. Feng, M. Chen, B. Hu, *J. Phys. Chem. Lett.* **2021**, *12*, 10346.

[81] a) K. Nishioka, K. Morimoto, T. Kusumoto, T. Harada, K. Kamiya, Y. Mukouyama, S. Nakanishi, *J. Am. Chem. Soc.* **2021**, *143*, 7394; b) Y. Zhang, L. Wang, X. Zhang, L. Guo, Y. Wang, Z. Peng, *Adv. Mater.* **2018**, *30*, 1705571; c) S. Samira, S. Deshpande, C. A. Roberts, A. M. Nacy, J. Kubal, K. Matesic´, O. Oesterling, J. Greeley, E. Nikolla, *Chem. Mater.* **2019**, *31*, 7300.

[82] a) B. Shi, K. Liu, E. Lee, C. Liao, in *Batteries: Materials Principles and Characterization Methods*, (Ed: C. Liao), IOP, Bristol, UK **2021**, Ch. 5; b) E. R. Ezeigwe, L. Dong, R. Manjunatha, Y. Zuo, S.-Q. Deng, M. Tan, W. Yan, J. Zhang, D. P. Wilkinson, *Nano Energy* **2022**, *95*, 106964.

[83] a) H. Kim, W.-J. Kwak, H.-G. Jung, Y.-K. Sun, *Energy Storage Mater.* **2019**, *19*, 148; b) D. Wang, X. Mu, P. He, H. Zhou, *Mater. Today* **2019**, *26*, 87.

[84] S. Yang, P. He, H. Zhou, *Energy Environ. Sci.* **2016**, *9*, 1650.

[85] L. Trotochaud, A. R. Head, O. Karslıoğlu, L. Kyhl, H. Bluhm, *J. Phys.: Condens. Matter* **2016**, *29*, 053002.

[86] Y. Wang, W. Wang, J. Xie, C.-H. Wang, Y.-W. Yang, Y.-C. Lu, *Nano Energy* **2021**, *83*, 105830.

[87] Y. Han, H. Zhang, Z. Yu, Z. Liu, *ACS Catal.* **2021**, *11*, 1464.

[88] a) J. Wu, T. Sharifi, Y. Gao, T. Zhang, P. M. Ajayan, *Adv. Mater.* **2019**, *31*, 1804257; b) S. Zhao, D. W. Wang, R. Amal, L. Dai, *Adv. Mater.* **2019**, *31*, 1801526; c) K. Zhao, X. Quan, *ACS Catal.* **2021**, *11*, 2076.

[89] A. Vasileff, C. Xu, Y. Jiao, Y. Zheng, S.-Z. Qiao, *Chem* **2018**, *4*, 1809.

[90] a) Y. Zhang, L. Tao, C. Xie, D. Wang, Y. Zou, R. Chen, Y. Wang, C. Jia, S. Wang, *Adv. Mater.* **2020**, *32*, 1905923; b) Q. Wang, Y. Lei, D. Wang, Y. Li, *Energy Environ. Sci.* **2019**, *12*, 1730.

[91] X. G. Wang, C. Wang, Z. Xie, X. Zhang, Y. Chen, D. Wu, Z. Zhou, *ChemElectroChem* **2017**, *4*, 2145.

[92] Z. Lian, Y. Lu, S. Ma, L. Wang, Z. Li, Q. Liu, *Chem. Eng. Sci.* **2022**, *450*, 138400.

[93] a) J. Li, H. Zhao, H. Qi, X. Sun, X. Song, Z. Guo, A. G. Tamirat, J. Liu, L. Wang, S. Feng, *Adv. Funct. Mater.* **2019**, *29*, 1806863; b) A. Khurram, M. He, B. M. Gallant, *Joule* **2018**, *2*, 2649.

[94] Z. Wang, F. Liu, X. Zeng, P. Dong, X. Li, Y. Zhang, *Ionics* **2021**, *27*, 2785.

[95] a) H. Yang, *Mater. Res. Bull.* **2021**, *142*, 111406; b) C. Bie, H. Yu, B. Cheng, W. Ho, J. Fan, J. Yu, *Adv. Mater.* **2021**, *33*, 2003521.

[96] D. Du, Z. Zhu, K.-Y. Chan, F. Li, J. Chen, *Chem. Soc. Rev.* **2022**, *51*, 1846.

[97] a) J. Li, K. Zhang, Y. Zhao, C. Wang, L. Wang, L. Wang, M. Liao, L. Ye, Y. Zhang, Y. Gao, *Angew. Chem., Int. Ed.* **2022**, *61*, e202114612; b) X. X. Wang, D. H. Guan, F. Li, M. L. Li, L. J. Zheng, J. J. Xu, *Small* **2021**, *17*, 2100642.

[98] D. H. Guan, X. X. Wang, M. L. Li, F. Li, L. J. Zheng, X. L. Huang, J. J. Xu, *Angew. Chem., Int. Ed.* **2020**, *59*, 19518.

[99] a) K. Khurana, N. Jaggi, *Plasmonics* **2021**, *16*, 981; b) C.-c. Jian, J. Zhang, W. He, X. Ma, *Nano Energy* **2021**, *82*, 105763.

[100] D.-H. Guan, X.-X. Wang, F. Li, L.-J. Zheng, M.-L. Li, H.-F. Wang, J.-J. Xu, *ACS Nano* **2022**, *16*, 12364.

[101] Q. Xu, L. Zhang, B. Cheng, J. Fan, J. Yu, *Chem* **2020**, *6*, 1543.

[102] Z. Zhang, Z. Zhang, P. Liu, Y. Xie, K. Cao, Z. Zhou, *J. Mater. Chem. A* **2018**, *6*, 3218.

[103] a) S. Zhang, Q. Fan, R. Xia, T. J. Meyer, *Acc. Chem. Res.* **2020**, *53*, 255; b) S. Tian, Y. Cao, T. Chen, S. Zang, J. Xie, *Chem. Commun.* **2020**, *56*, 1163.

[104] K. J. Fisher, K. L. Materna, B. Q. Mercado, R. H. Crabtree, G. W. Brudvig, *ACS Catal.* **2017**, *7*, 3384.

[105] X. Yu, A. Manthiram, *Small Struct.* **2020**, *1*, 2000027.

[106] B. Liu, W. Xu, P. Yan, S. T. Kim, M. H. Engelhard, X. Sun, D. Mei, J. Cho, C. M. Wang, J. G. Zhang, *Adv. Energy Mater.* **2017**, *7*, 1602605.

[107] B. Liu, W. Xu, P. Yan, X. Sun, M. E. Bowden, J. Read, J. Qian, D. Mei, C. M. Wang, J. G. Zhang, *Adv. Funct. Mater.* **2016**, *26*, 605.

[108] O. Wijaya, P. Hartmann, R. Younesi, I. I. Markovits, A. Rinaldi, J. Janek, R. Yazami, *J. Mater. Chem. A* **2015**, *3*, 19061.

[109] W. Xie, X. Ji, X. Feng, X. Lu, *AIChE J.* **2015**, *61*, 4437.

[110] J. Xiao, H. Sun, M. Yu, T. Zhang, J. Li, *AIP Adv.* **2020**, *10*, 115217.

[111] K. Yang, R. Kas, W. A. Smith, *J. Am. Chem. Soc.* **2019**, *141*, 15891.

[112] W. Gao, Z. D. Hood, M. Chi, *Acc. Chem. Res.* **2017**, *50*, 787.

[113] Q.-J. Fang, J.-k. Pan, W. Zhang, F.-l. Sun, W.-x. Chen, Y.-f. Yu, A.-F. Hu, G.-l. Zhuang, *J. Colloid Interface Sci.* **2022**, *617*, 752.

[114] a) Z. Sun, H. Yin, K. Liu, S. Cheng, G. K. Li, S. Kawi, H. Zhao, G. Jia, Z. Yin, *SmartMat* **2022**, *3*, 68; b) J. Liu, W. Luo, L. Wang, J. Zhang, X. Z. Fu, J. L. Luo, *Adv. Funct. Mater.* **2022**, *32*, 2110748.

[115] E. W. Lees, B. A. Mowbray, F. G. Parlane, C. P. Berlinguette, *Nat. Rev. Mater.* **2021**, *7*, 55.

[116] K. Deng, Q. Zeng, D. Wang, Z. Liu, G. Wang, Z. Qiu, Y. Zhang, M. Xiao, Y. Meng, *Energy Storage Mater.* **2020**, *32*, 425.

Shilin Zhang is now a research fellow at the University of Adelaide, Adelaide, Australia. He received his Ph.D. degree from the Institute of Superconducting & Electronic Materials in the University of Wollongong (Australia) in 2020 under the supervision of Prof. Zaiping Guo. His current research interests focus on the design, synthesis, and characterization of materials in the field of electrochemical devices such as ion batteries and metal–air batteries.

Zaiping Guo is currently a professor at the School of Chemical Engineering and Advanced Materials, the University of Adelaide. She obtained her Ph.D. from the University of Wollongong in 2003. She was a distinguished professor in the School of Mechanical, Materials, Mechatronic, and Biomedical Engineering, University of Wollongong before joining the University of Adelaide. Her research is focused on the design and application of electrode materials and electrolytes for energy storage and conversion.